Research Square

Preprints are preliminary reports that have not undergone peer review.
They should not be considered conclusive, used to inform clinical practice,
or referenced by the media as validated information.

Quantum enhancement and Doppler-induced suppression in a Kasevich--Chu atom interferometer with motional squeezed states

Dongyang Yu

doangy.zsr@gmail.com

Zhejiang University of Technology

Yubin Wang

Zhejiang University of Technology

Chenwei Lv

Southern University of Science and Technology

Fong En Oon

Zhejiang University of Technology

Qiang Lin

Zhejiang University

Article

Keywords:

Posted Date: August 19th, 2026

DOI: https://doi.org/10.21203/rs.3.rs-10493536/v1

License: This work is licensed under a Creative Commons Attribution 4.0 International License.
Read Full License

Additional Declarations: No competing interests reported.

Quantum enhancement and Doppler-induced suppression in a Kasevich–Chu atom interferometer with motional squeezed states

Dongyang Yu,[1,2,*] Yubin Wang,[1,2] Chenwei Lv,[3] Fong En Oon,[1,2] and Qiang Lin[4]

[1] *School of Physics and Optical Engineering, Zhejiang University of Technology, No. 288, Liuhe Road, Hangzhou, 310023, China*

[2] *Zhejiang Provincial Key Laboratory and Collaborative Innovation Center for Quantum Precise Measurement, Zhejiang University of Technology, No. 288, Liuhe Road, Hangzhou, 310023, China*

[3] *State Key Laboratory of Quantum Functional Materials, Department of Physics, and Guangdong Basic Research Center of Excellence for Quantum Science, Southern University of Science and Technology, Shenzhen, China*

[4] *State Key Laboratory of Ocean Sensing and Institute of Quantum Sensing and School of Physics, Zhejiang University, Hangzhou, 310027, China*

(Dated: July 27, 2026)

The intrinsic hybridization of internal and external atomic degrees of freedom in a Kasevich–Chu interferometer enables engineered motional fluctuations to serve as an independent metrological resource while preserving standard-quantum-limit scaling. We develop a unified computational framework, based on quantum and classical Fisher information, for arbitrary uncorrelated motional inputs under both ideal and Doppler-modified atom–light interactions; a hybrid numerical integration scheme makes the highly oscillatory joint population–position calculation tractable. Applied to single-mode motional squeezed states, the framework predicts up to a twofold sensitivity gain over the semiclassical limit for population measurement through an enlarged atomic coherence length. Joint population–position measurement additionally exploits squeezing-induced reshaping of the spatial interference fringes, yielding substantial gains over a broader parameter regime and exceeding threefold in the quantum-enhancement-dominated regime. This enhancement remains robust to Doppler-induced pulse imperfections under strong momentum broadening and finite spatial resolution, while an optimal squeezing strength emerges from the competition between quantum enhancement and Doppler-induced suppression. Our results establish external motional fluctuations as a robust and underexplored single-particle resource for quantum-enhanced atom interferometry and provide a basis for extensions to correlated many-body systems.

I. INTRODUCTION

Owing to their high sensitivity and stability [1–4], the Kasevich–Chu (KC) atom interferometer, based on matter-wave interference [5, 6], offers significant scientific value and engineering advantages, with applications in geophysics, mineral exploration, and inertial navigation [7–11]. A promising route toward higher sensitivity is to exploit many-body entanglement in ultracold atom interferometers, i.e., spin squeezing [12–14], squeezing of well-separated momentum modes [15, 16] and beyond. Properly engineered entangled atomic ensembles provide sensing capabilities beyond the standard quantum limit and, in principle, allow sensitivities approaching the Heisenberg limit, $\delta g \propto 1/N$. Typical implementations employ one-axis or two-axis twisting Hamiltonians [12], realized using optical cavities [17], spin-exchange interactions in spinor Bose–Einstein condensates [2, 18, 19], or intercomponent interactions in two-component condensates [20–22]. Nevertheless, the preparation and readout of many-body entangled states remain experimentally challenging owing to their fragility against noise. Furthermore, the sensitivity gains demonstrated to date remain relatively limited compared with those of conventional uncorrelated cold-atom interferometers, which are broadly deployed on various platforms worldwide.

Uncorrelated cold-atom ensembles are still widely used, especially in mobile platforms where atomic phase coherence is fragile, because they offer a practical trade-off between achieving high sensitivity and maintaining a large dynamical bandwidth [23]. According to Fisher information theory, the sensitivity scales as $\delta g \propto 1/(\sqrt{N}k_0(T/2)^2)$, corresponding to the standard quantum limit. Common strategies for systematically enhancing the sensitivity [18, 24–29] include improving the atomic phase coherence (e.g., suppressing vibration noise), increasing effective recoil momentum $\hbar k_0$ and interrogation time T, and enlarging the atom flux N. Progress along these directions is currently constrained by various experimental limitations.

However, most existing studies overlook a key feature of a KC atom interferometer: unlike its optical counterparts [30, 31], its interferometric arms are formed through the hybridization of the internal and external atomic degrees of freedom, analogous to spin–orbit coupling, which plays a central role in many areas of condensed-matter physics [32]. Consequently, in addition to using the internal degree of freedom to generate spin squeezing or many-body entanglement, one may exploit quantum fluctuations of the external motional degree of freedom as an independent metrological resource already at the single-particle level. Indeed, as indicated in Ref. [33], suit-

* doangy.zsr@gmail.com

ably engineered single-particle quadrature fluctuations may enhance the sensitivity of a KC atom interferometer. These external fluctuations encompass position and momentum fluctuations as well as their correlations, which jointly influence the wave-packet overlap, spatial distribution, and interference pattern.

Several routes are available for engineering such external fluctuations. For instance, when engineering spin squeezing in two-component Bose–Einstein condensates in a KC atom gravimeter, strong spin squeezing is always accompanied by substantial momentum broadening in the unavoidable free-expansion dynamics [22, 34, 35]. Moreover, such fluctuations can also be directly engineered by preparing motional squeezed states (MSSs) [36]. At the single-particle level, single-mode or two-mode MSSs can be readily generated experimentally using frequency-jump modulation schemes [37–41], and even truncated MSSs can be spontaneously induced with the assistance of Bose–Einstein condensates [42]. MSSs have demonstrated broad significance across several platforms, including Rydberg atoms [43, 44], trapped ions [37, 40, 45], and photonic systems [46], where they enable enhanced control over quantum fluctuations and correlations. In quantum optics, the counterpart of a MSS is a squeezed-vacuum state, which can be represented as a Perelomov SU(1,1) coherent state and plays a central role in precision measurements of extremely weak signals [30, 46, 47]. Interestingly, the collective breathing dynamics of two-dimensional interacting Bose gases share the same SU(1,1) dynamical symmetry, foreshadowing the many-body extension discussed below [48, 49].

To date, MSSs have received little attention in atom interferometry [50, 51], particularly in KC atom gravimeters. Their use is hindered by a fundamental tension: the same motional fluctuations that can enhance sensitivity generally also broaden the momentum distribution, producing velocity-dependent Doppler shifts and imperfect beam-splitter and mirror operations [52, 53]. For spatially resolved readout, both MSS and free expansion dynamics induce position–momentum correlations and reshape the interference fringes that carry additional information about the encoded parameter. Once the momentum dependence of the atom–light coupling is retained, however, the corresponding Fisher-information integrals become highly oscillatory and difficult to evaluate accurately and efficiently. A systematic treatment that connects ideal and realistic atom–light interactions, compares experimentally accessible readouts, and quantitatively resolves motional enhancement and Doppler-induced degradation has therefore been lacking.

Here we develop a unified single-particle framework for arbitrary uncorrelated motional input states that covers both ideal and Doppler-modified atom–light interactions. In the ideal limit, the QFI and the CFIs associated with population and joint population–position measurements admit analytical formulations. For non-ideal interactions, which must be retained for strongly momentum-broadened states, we derive a comprehensive computational framework for evaluating the QFI and the CFI of both readouts. In the most demanding case of spatially resolved joint measurement, the highly oscillatory integrals are rendered tractable by a hybrid scheme combining domain decomposition, Gauss–Legendre quadrature, and Levin-type quadrature [54, 55]. This unified description allows us to quantify, on the same footing, the sensitivity gain generated by motional squeezing, the relative performance of the two measurement protocols, their control-parameter optimization where computationally feasible, and the degradation caused by Doppler effects. Applied to single-mode MSSs, the framework predicts a sensitivity gain of up to twofold for population measurement and exceeding threefold for joint population–position measurement in the quantum-enhancement-dominated regime. The latter gain remains robust under strong momentum broadening and finite spatial detection resolution, while an optimal squeezing strength emerges in the crossover between quantum enhancement and Doppler-induced degradation. Although the single-particle gains demonstrated here remain moderate and retain standard-quantum-limit scaling, the framework provides a systematic basis for extensions to correlated many-body inputs, where collective quantum correlations may support substantially larger gains.

The rest of this manuscript is organized as follows. In Sec. II, we derive a unified computational framework for the QFI and CFI of two commonly deployed measurement protocols. In Sec. III, we use this framework to analyze the sensitivity of a KC atom interferometer with an MSS as input, demonstrate both the sensitivity enhancement from quantum quadrature fluctuations and the corresponding Doppler-induced suppression caused by large momentum broadening, and assess the experimental feasibility. In Sec. IV, we present our conclusions and outlook.

II. COMPUTATIONAL FRAMEWORK OF QUANTUM AND CLASSICAL FISHER INFORMATION

Thermal Doppler broadening is a well-known limitation in conventional KC atom gravimeters. Here, however, the momentum broadening originates from deliberately engineered quantum fluctuations of the input motional state rather than from thermal excitations. To account explicitly for Doppler effects, we formulate the KC unitary evolution in both the “Ideal” and “Doppler” scenarios and establish a unified framework for evaluating the corresponding QFI and CFI. The “Ideal” scenario assumes perfect light pulses, whereas the “Doppler” scenario retains the momentum-dependent pulse imperfections induced by Doppler broadening. For the latter, we employ our SU(2) Lie group formalism to derive a generic unitary evolution operator $\hat{U}_{\mathrm{KC}}$. It should be noted that we do not address the problem of optimal

measurements associated with MSSs here; the rationale will be discussed later. Without loss of generality, the input state of a KC atom interferometer can be written as a product of an internal state $|a\rangle$ and an external state $|\Psi_0\rangle$, namely $|a\rangle|\Psi_0\rangle$. The final state is then given by the unitary evolution $|\Psi(t)\rangle = \hat{U}_{\rm KC}|a\rangle|\Psi_0\rangle$, where the gravitational acceleration g is encoded into the output state via the Hamiltonian. Since in our case the transverse motion does not affect the sensitivity, we restrict our analysis to the direction along the linear gravitational potential.

A. Quantum Fisher information

The QFI determines the quantum Cramér–Rao bound (QCRB) [56] on the sensitivity. For N uncorrelated particles, this bound is $\delta g \geq 1/\sqrt{NF_Q}$, where $F_Q = 4(\langle\partial_g\Psi(t)|\partial_g\Psi(t)\rangle - |\langle\Psi(t)|\partial_g\Psi(t)\rangle|^2)$ denotes the single-particle QFI. To isolate the role of Doppler effects, we consider two scenarios, "Ideal" (denoted by $\mathcal{S} = \mathcal{I}$) and "Doppler" ($\mathcal{S} = \mathcal{D}$), as introduced above. In both scenarios, the evolution operator can be written as follows,

$$\begin{aligned} \hat{U}^{\mathcal{S}}_{\rm KC} &= \hat{V}^{\mathcal{S}}_3\hat{U}_g(T_2)\hat{V}^{\mathcal{S}}_2\hat{U}_g(T_1)\hat{V}^{\mathcal{S}}_1, \\ \hat{V}^{\mathcal{S}}_j &= \hat{U}_0\tilde{U}^{\mathcal{S}}_j\hat{U}^{\dagger}_0. \end{aligned} \tag{1}$$

Here $\hat{U}_0 = |a\rangle\langle a|\exp(-ik_0\hat{z}/2) + |b\rangle\langle b|\exp(ik_0\hat{z}/2)$ and $\hat{U}^{\dagger}_0$ together describe the momentum transfer ($\hbar k_0$) from the pulsed laser, while $\hat{U}_g(T_{1,2})$ describes free fall and expansion in the gravitational potential,

$$\hat{U}_g(T_{1,2}) = \hat{U}_p(T_{1,2})\exp(ig\hat{G}(T_{1,2})), \tag{2}$$

$$\hat{G}(T) = \frac{mT}{\hbar}\hat{z} + \frac{T^2}{2\hbar}\hat{p}, \tag{3}$$

$\hat{U}_p(T_{1,2}) = \exp(-i\frac{T_{1,2}}{\hbar}\frac{\hat{p}^2}{2m})$. T_1 and T_2 denote as the first and second interrogation times, respectively, with $T_1 + T_2 = T$ throughout. For the conventional atom–light interaction, the frequency shift associated with the momentum broadening of the input state is negligible, that is $\Delta pk_0/m \ll \Omega$. Then $\tilde{U}^{\mathcal{I}}_j$ can be written as follows,

$$\begin{aligned} \tilde{U}^{\mathcal{I}}_j &= \cos(\Omega\tau_j/2)\hat{I} \\ &\quad -i\sin(\Omega\tau_j/2)\cdot\left(e^{i\phi_j}|a\rangle\langle b| + e^{-i\phi_j}|b\rangle\langle a|\right), \end{aligned} \tag{4}$$

$\Omega\tau_j = \pi/2$ and π (Ω is the Rabi frequency) correspond to the $\pi/2$ and π pulses, respectively. Here ϕ_j is the phase of the jth pulsed laser, and $|a\rangle$ and $|b\rangle$ denote the two internal states. However, this evolution operator (Eq. 4) becomes inaccurate for input states with large momentum broadening, i.e., $\Delta pk_0/m \gtrsim \Omega$. According to our previous framework based on SU(2) Lie group theory [57], the unitary operator $\tilde{U}^{\mathcal{D}}_j$ describing the imperfect interaction between pulsed lasers and a two-level atom in the "Doppler" scenario can be expressed as

$$\tilde{U}^{\mathcal{D}}_j(\hat{p}) = \hat{U}^{\mathcal{D}}_j(\hat{p} - mgt), \tag{5}$$

with

$$\begin{aligned} \hat{U}^{\mathcal{D}}_j(\hat{p}) &= \left(\hat{A}_j + i\hat{B}_j\right)|a\rangle\langle a| + \left(\hat{A}_j - i\hat{B}_j\right)|b\rangle\langle b| \\ &\quad -i\hat{C}_j\left(\exp(i\phi_j)|a\rangle\langle b| + \exp(-i\phi_j)|b\rangle\langle a|\right), \end{aligned} \tag{6}$$

$\hat{A}_j = \cos(\hat{\Delta}\tau_j/2)$, $\hat{B}_j = \hat{b}_0/\hat{\Delta}\sin(\hat{\Delta}\tau_j/2)$ and $\hat{C}_j = \Omega/\hat{\Delta}\sin(\hat{\Delta}\tau_j/2)$ with $\hat{\Delta} = \sqrt{\hat{b}_0^2 + \Omega^2}$, $\hat{b}_0 = k_0\hat{p}/m + \delta_0$ with the initial detuning δ_0. Here it is worth noting that Eq. 5 is valid when the chirping of the pulsed-laser frequency is $\delta(t) = \delta_0 - k_0gt$, which exactly compensates for the Doppler shift arising from the uniform acceleration of atoms in a linear potential [58]. It is straightforward to see that when the Rabi frequency Ω is much larger than all other typical frequency scales, i.e., $\Delta pk_0/m$, Eq. (5) reduces to Eq. (4).

In the "Ideal" scenario, the single-particle QFI $F_{\rm Q} = F^{\mathcal{I}}_{\rm Q}$ can be written as follows [33],

$$F^{\mathcal{I}}_{\rm Q} = k_0^2\left(\frac{T^2}{2} - T_2^2\right)^2 + 4{\rm Var}\left(\hat{G}(T)\right), \tag{7}$$

where ${\rm Var}(\cdot)$ denotes the variance. Evidently, increasing either term on the right-hand side of Eq. 7 increases the QFI and therefore lowers the QCRB, ultimately enhancing the sensitivity of KC atom interferometry. However, the first term originates from the phase coherence of the two interference arms, while the second term stems from the external quantum fluctuations of the input state. For the "Doppler" scenario, the calculation of the QFI is lengthy. We therefore display only the final result here; details are provided in the Appendix A,

$$F^{\mathcal{D}}_{\rm Q} = k_0^2\left(\frac{T^2}{2} - T_2^2\right)^2 + 4\langle\Psi_0|\hat{G}''|\Psi_0\rangle + 4{\rm Var}(\hat{G}'). \tag{8}$$

$\hat{G}' = \hat{d}_{0,0} + \frac{mT}{\hbar}\hat{z}$, where both $\hat{d}_{0,0}$ and $\hat{G}''$ are operators defined in momentum space, also listed in the Appendix A. In the limit $\Omega \to \infty$, $\hat{G}'' \to 0$ and ${\rm Var}(\hat{G}') \to {\rm Var}\left(\hat{G}(T)\right)$, which coincides with the result in the "Ideal" scenario, that is, $\lim_{\Omega\to\infty} F^{\mathcal{D}}_{\rm Q} = F^{\mathcal{I}}_{\rm Q}$. When the quantum fluctuations of the input state are neglected and *interrogation-time symmetry* $T_1 = T_2 = T/2$ is imposed, both Eq. 7 and Eq. 8 consistently output the semiclassical limit (SCL), $F_{\rm SCL} = k_0^2(T/2)^4$ which determines the standard quantum limit of a conventional symmetric KC atom interferometer with negligible motional enhancement,

$$\delta g_{\rm SCL} = \frac{1}{\sqrt{NF_{\rm SCL}}}. \tag{9}$$

Comparing the QFIs in the "Doppler" and "Ideal" scenarios, two distinct features in the "Doppler" case are summarized here and the details are also given in the Appendix A. First, the external quantum fluctuations ($\hat{G}'$ and $\hat{G}''$) in the "Doppler" scenario depend on both interrogation times T_1 and T_2, rather than the total time $T = T_1 + T_2$. Second, the QFI in Eq. 8 is weakly affected

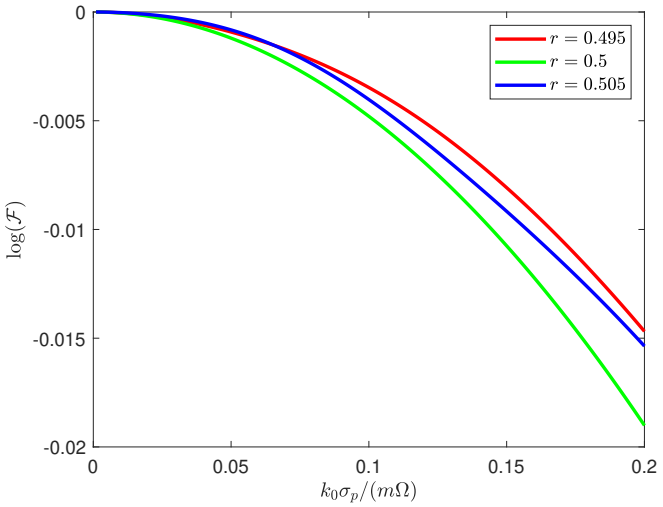


FIG. 1. (color online) Root fidelity $\mathcal{F}$ versus momentum broadening σ_p for an input Gaussian wave packet $\langle p|\Psi_0\rangle \propto \exp(-p^2/(2\sigma_p^2))$. The solid red, green and blue lines correspond to the interrogation-time ratio $r = 0.495$, 0.5 and 0.505, respectively. Here $\delta_0 = -E_r$, $\Omega = 20E_r/\hbar$, $T = 200\hbar/E_r$, $\phi_1 - \phi_2 = \pi/4$, $\phi_2 - \phi_3 = -\pi/4$.

by the gravitational acceleration g and by the phase difference of the pulsed lasers through a phase $\hat{\Theta}$ (defined in momentum space),

$$\hat{\Theta} = \phi_1 - \phi_2 + \frac{k_0 T_1}{m}(\hat{p} + \frac{\hbar k_0}{2}) + \frac{g k_0 T_1^2}{2}. \tag{10}$$

While increasing the momentum broadening may increase the QFI and thereby enhance the sensitivity through Eq. 7 and Eq. 8, it also causes a fraction of atoms to deviate from the main interference paths of a KC atom interferometer [59]. As a result, the number of atoms that actually participate in the KC interferometer is reduced, eventually weakening the sensitivity gain brought by the increased momentum fluctuation. To quantitatively characterize this phenomenon, we introduce the root fidelity between two scenarios, defined as $\mathcal{F} = |\langle\Psi_0|\langle a|\hat{U}_{\rm KC}^{\mathcal{I}\dagger}\hat{U}_{\rm KC}^{\mathcal{D}}|a\rangle|\Psi_0\rangle|$, which quantifies the light-pulse imperfections induced by Doppler broadening,

$$\begin{aligned}\mathcal{F} \;=\; & |\langle\Psi_0|\langle a|e^{-i\frac{k_0\hat{z}}{2}}\tilde{U}_1^{\mathcal{I}\dagger}e^{-i\hat{\beta}_1\sigma_z}\tilde{U}_2^{\mathcal{I}\dagger}e^{-i\hat{\beta}_2\sigma_z}\tilde{U}_3^{\mathcal{I}\dagger} \\ & \hat{U}_3^{\mathcal{D}}e^{i\hat{\beta}_2\sigma_z}\hat{U}_2^{\mathcal{D}}e^{i\hat{\beta}_1\sigma_z}\hat{U}_1^{\mathcal{D}}e^{i\frac{k_0\hat{z}}{2}}|a\rangle|\Psi_0\rangle|,\end{aligned} \tag{11}$$

where $\hat{\beta}_1 = gk_0T_1^2/4 + k_0T_1\hat{p}/(2m)$ and $\hat{\beta}_2 = gk_0(T_1^2 + 2T_1T_2)/4 + k_0T_2\hat{p}/(2m)$. For intuition, we show the evolution of $\mathcal{F}$ versus momentum broadening σ_p in Fig. 1 using a standard Gaussian wave packet as input, $\langle p|\Psi_0\rangle \propto \exp(-p^2/(2\sigma_p^2))$. As shown, the root fidelity $\mathcal{F}$ decays with increasing σ_p faster than an exponential trend while the interrogation-time ratio $r \equiv T_1/T$ (used throughout this work) only slightly modifies the decay.

B. Classical Fisher Information

For N uncorrelated particles, the classical Cramér–Rao bound of a chosen measurement protocol is given as

$$\delta g_{\rm C} = \frac{1}{\sqrt{NF_{\rm C}}}, \tag{12}$$

and ultimately bounded by the QCRB $\delta g_{\rm C} \geq 1/\sqrt{NF_{\rm Q}}$ when the measurement protocol is optimal. For clarity, we quantify the sensitivity gain of a chosen measurement under specified control parameters as

$$\mathcal{G} = \frac{\delta g_{\rm SCL}}{\delta g_{\rm C}} = \sqrt{\frac{F_{\rm C}}{F_{\rm SCL}}}. \tag{13}$$

Accordingly, a larger CFI $F_{\rm C}$ yields lower classical Cramér–Rao bound and hence a higher sensitivity gain for the chosen measurement protocol throughout this work.

In the "Ideal" scenario, it has been pointed out in the literature that applying a harmonic potential before measurement to implement an appropriate phase-space rotation can enable an optimal measurement [33, 57]. However, this scheme is difficult to generalize to the "Doppler" scenario, namely to an input MSS with large momentum broadening. Three main challenges arise here: (i) Due to the finite momentum transfer of pulsed lasers ($\hbar k_0$), a spin-dependent momentum kick is required to eliminate the velocity difference between different internal states; this operation becomes difficult to implement in the presence of large momentum broadening. (ii) Because of unavoidable free expansion, the spatial extent of the atomic cloud can become too large to apply a suitable harmonic trapping potential prior to measurement. (iii) The Doppler effect can, to some extent, degrade the universality of the phase-space rotation operation [57]. Taking these facts into account, we do not address the problem of optimal measurement for MSSs in this work. Instead, we focus on two types of experimentally feasible measurements: population measurement (denoted by $\{\hat{S}_z\}$ throughout this work) and joint population–position measurement ($\{\hat{z}, \hat{S}_z\}$). We then explicitly obtain the unified computational framework of CFI for arbitrary momentum or position fluctuations, as presented in the following two subsections.

1. *Population measurement and classical Fisher information*

Population measurement is the most commonly employed readout scheme in practical atom interferometry. Its performance can be quantified by the corresponding CFI, $F_{\rm C}^{\mathcal{I},\mathcal{D}}(\{\hat{S}_z\}) = \sum_{s=a}^{b}(\partial_g P_s)^2/P_s$, where the information on g is encoded in the probabilities P_s of $|a\rangle$ and $|b\rangle$.

In the "Ideal" scenario, the probabilities can be written analytically as $P_{a/b} = (1 \pm \mathcal{C}\cos(\varphi))/2$ with $\varphi = \Phi - \phi_f -$

ϕ_g, here $\Phi = \phi_1 - 2\phi_2 + \phi_3$, $\phi_f = E_r(T_2 - T_1)/\hbar$ and $\phi_g = \frac{gk_0}{2}(T^2 - 2T_1^2)$ denote the total laser phase difference, the phase shift from the momentum kicks of the pulsed lasers, and the phase shift from the linear gravitational potential, respectively. Here $E_r = \hbar^2 k_0^2/(2m)$ denotes the recoil energy induced by pulsed lasers. The CFI in the "Ideal" scenario is therefore,

$$F_C^{\mathcal{I}}(\{\hat{S}_z\}) = \frac{k_0^2(T^2 - 2T_1^2)^2}{4}\mathcal{C}^2, \tag{14}$$

where the optimal phase difference $\Phi^{\mathcal{I}}(\{\hat{S}_z\}) = \phi_f + \phi_g + \pi/2$ is set, and the interference contrast is

$$\mathcal{C} = \langle\Psi_0|\exp(i\frac{k_0}{m}(T_2 - T_1)\hat{p})|\Psi_0\rangle. \tag{15}$$

The latter represents the wavefunction overlap between the distinct interference arms.

In the "Doppler" scenario, although the expressions for the probabilities $P_{a/b}$ are lengthy, the CFI can still be written explicitly as

$$F_C^{\mathcal{D}}(\{\hat{S}_z\}) = \frac{k_0^2 T^4}{4}\sum_s \frac{\left(M_s + r^2 N_s\right)^2}{P_s}, \tag{16}$$

here

$$\begin{aligned} P_s &= \langle\Psi_0|\hat{K}_{sa}^\dagger \hat{K}_{sa}|\Psi_0\rangle, \\ M_s &= \frac{i}{2}\langle\Psi_0|\hat{K}_{sa}^\dagger \hat{K}'_{sa} - \hat{K}'^\dagger_{sa}\hat{K}_{sa}|\Psi_0\rangle, \\ N_s &= \frac{i}{2}\langle\Psi_0|\hat{K}_{sa}^\dagger \hat{K}''_{sa} - \hat{K}''^\dagger_{sa}\hat{K}_{sa}|\Psi_0\rangle. \end{aligned} \tag{17}$$

and

$$\begin{aligned} \hat{K}_{sa} &= e^{-i\frac{k_0\hat{z}}{2}}\langle s|\hat{U}_3^{\mathcal{D}} e^{i\hat{\beta}_2\sigma_z}\hat{U}_2^{\mathcal{D}} e^{i\hat{\beta}_1\sigma_z}\hat{U}_1^{\mathcal{D}}|a\rangle e^{i\frac{k_0\hat{z}}{2}}, \\ \hat{K}'_{sa} &= e^{-i\frac{k_0\hat{z}}{2}}\langle s|\hat{U}_3^{\mathcal{D}} e^{i\hat{\beta}_2\sigma_z}\sigma_z\hat{U}_2^{\mathcal{D}} e^{i\hat{\beta}_1\sigma_z}\hat{U}_1^{\mathcal{D}}|a\rangle e^{i\frac{k_0\hat{z}}{2}}, \\ \hat{K}''_{sa} &= e^{-i\frac{k_0\hat{z}}{2}}\langle s|\hat{U}_3^{\mathcal{D}} e^{i\hat{\beta}_2\sigma_z}[\hat{U}_2^{\mathcal{D}}, \sigma_z] e^{i\hat{\beta}_1\sigma_z}\hat{U}_1^{\mathcal{D}}|a\rangle e^{i\frac{k_0\hat{z}}{2}}, \end{aligned} \tag{18}$$

$\sigma_z = [1, 0; 0, -1]$ is the third Pauli matrix. A similar equivalence can be proven in the limit $\Omega \to \infty$, $\lim_{\Omega\to\infty} F_C^{\mathcal{D}}(\{\hat{S}_z\}) = F_C^{\mathcal{I}}(\{\hat{S}_z\})$.

2. *Joint population–position measurement and classical Fisher information*

Compared with population measurement, joint population–position measurement enables substantial better performance and more possibilities in a KC atom interferometer because it also uses information contained in the spatial distribution. Such measurements have been widely investigated in point-source and phase-shear interferometry [60–63]. In phase-shear interferometry, the interferometric phase is mapped onto the spatial probability distribution, enabling simultaneous estimation of rotation and the gravitational-field gradient through phase shear and interrogation-time asymmetry in the transverse and longitudinal directions, respectively. The single-particle CFI of joint population–position measurement is evaluated from the probability distribution $P_s(z)$ with $P_s(z) = |L_s(z)|^2$,

$$L_s(z) = \langle z - z_0|\hat{K}_{sa}\hat{U}_p(T)|\Psi_0\rangle. \tag{19}$$

Here $z_0 = \frac{gT^2}{2} + \frac{\hbar k_0 T}{2m}$ represents the mean output position due to free fall and the drift induced by momentum kicks. By definition, the CFI can be written as $F_C^{\mathcal{I},\mathcal{D}}(\{\hat{z}, \hat{S}_z\}) = \sum_{s=a}^{b}\int dz \frac{(\partial_g P_s(z))^2}{P_s(z)}$, and simplified as follows,

$$F_C^{\mathcal{I},\mathcal{D}}(\{\hat{z}, \hat{S}_z\}) = \sum_{s=a}^{b}\int dz \frac{k_0^2 T^4}{4L_s^* L_s}\left(\mathrm{Im}(L_s H_s^*)\right)^2, \tag{20}$$

here

$$H_s(z) = \langle z|\Big(\hat{K}'_{sa} - \frac{2\hat{p}}{\hbar k_0}\hat{K}_{sa} + r^2\hat{K}''_{sa}\Big)\hat{U}_p(T)|\Psi_0\rangle. \tag{21}$$

In the "Ideal" scenario, it can be proven that $\lim_{\Omega\to\infty} F_C^{\mathcal{D}}(\{\hat{z}, \hat{S}_z\}) = F_C^{\mathcal{I}}(\{\hat{z}, \hat{S}_z\})$.

We emphasize that the two scenarios differ in their dependence on the pulsed-laser phases. In the "Ideal" scenario, both CFIs (Eq. 14 and Eq. 20) depend on the total phase difference $\Phi = \phi_1 - 2\phi_2 + \phi_3$, while in the "Doppler" scenario, both CFIs (Eq. 16, Eq. 20) depend separately on $\psi_{12} = \phi_1 - \phi_2$ and $\psi_{23} = \phi_2 - \phi_3$.

III. ENHANCED SENSITIVITY AND DOPPLER-INDUCED SUPPRESSION OF MOTIONAL SQUEEZED STATES

Assuming that the atoms are prepared in a one-dimensional harmonic trapping potential, we take the external input state $|\Psi_0\rangle$ to be an MSS, which can be expressed by the squeezing operator acting on the vacuum state $|0\rangle$ of a harmonic trapping potential, $|\Psi_0\rangle = \exp(\xi\hat{a}^{\dagger 2}/2 - \xi^*\hat{a}^2/2)|0\rangle$ [47, 51], $\xi = \beta\exp(i\theta)$, here $\hat{a}$ and $\hat{a}^\dagger$ are the annihilation and creation operators of a harmonic potential, respectively. The MSS in momentum space can be written as follows,

$$\langle p|\Psi_0\rangle = \frac{(1 - |\alpha|^2)^{1/4}}{\sqrt{\sigma_p\sqrt{\pi}}\sqrt{1-\alpha}} e^{\left(-\frac{1+\alpha}{2(1-\alpha)}\frac{p^2}{\sigma_p^2}\right)}, \tag{22}$$

where $\alpha = \tanh(\beta)e^{i\theta}$ is the parameter defined on the Poincaré disk, $|\alpha| \le 1$. As we will see in Sec. III B and Appendix B, both nonzero $\mathrm{Im}(\alpha)$ and free-expansion dynamics induce a nontrivial Gaussian wave packet of either output ($s = a$ or b) with position–momentum correlations, which can be written as

$$\langle s|\langle p|\Psi(T)\rangle \propto \exp(-(iA + B)p^2), \tag{23}$$

where $A \in \mathcal{R}$ and $B > 0$ (see Appendix B). Here the quadratic momentum phase in Eq. 23 plays an essential role for position-based measurement. The squeezing strength and angle in phase space are controlled by (β, θ). $\sigma_p = \sqrt{m\hbar\omega}$, where ω is the frequency of the initial harmonic trap and sets the initial momentum broadening. The momentum and position uncertainties (broadenings) of an MSS, Δp and Δz, can be written as follows,

$$\Delta p = \frac{\sigma_p}{\sqrt{2}} \frac{|1-\alpha|}{\sqrt{1-|\alpha|^2}}, \tag{24}$$

$$\Delta z = \frac{\hbar}{\sqrt{2}\sigma_p} \frac{|1+\alpha|}{\sqrt{1-|\alpha|^2}}, \tag{25}$$

Correspondingly, the position-momentum uncertainty product is $\Delta p(\alpha)\Delta z(\alpha) = \hbar|1-\alpha^2|/(2(1-|\alpha|^2))$. Each quadrature fluctuation is symmetric about the real axis of α ($\mathrm{Im}(\alpha) = 0$), where the uncertainty product attains its minimum value. Around $\alpha = 1$, the position uncertainty is strongly enhanced while the momentum uncertainty is suppressed; the opposite behavior occurs around $\alpha = -1$. Therefore, the "Doppler" scenario is essential near $\alpha = -1$, whereas the "Ideal" scenario is sufficient near $\alpha = 1$. The tunable squeezing of MSSs enables us to investigate the quantum external fluctuations of the input state.

Before discussing the CFIs of two chosen measurement protocols, it is useful to discuss the corresponding QFIs in the two scenarios. In the "Ideal" scenario, the contribution from the quantum fluctuations of the input MSS can be calculated analytically,

$$\frac{8\mathrm{Var}(\hat{G})}{k_0^2 T^4} = \Big(\frac{\sigma_p}{\hbar k_0}\sin(\theta/2) + \frac{\sigma_T}{\sigma_p}\cos(\theta/2)\Big)^2 e^{2\beta} + \Big(\frac{\sigma_p}{\hbar k_0}\cos(\theta/2) - \frac{\sigma_T}{\sigma_p}\sin(\theta/2)\Big)^2 e^{-2\beta}. \tag{26}$$

$\sigma_T = 2m/(k_0 T)$, where $\hbar/\sigma_T$ quantifies the position uncertainty of output atoms induced by the momentum kicks in the freely falling frame. The QFI can clearly be exponentially enhanced along an appropriate direction on the Poincaré disk. For a fixed β, $F_Q^{\mathcal{I}}$ in Eq. 7 achieves the maximum and minimum when $\theta = (\theta_c, \theta_c + \pi)$,

$$\mathrm{Var}(\hat{G}(T))\Big|_{\mathrm{Min}}^{\mathrm{Max}} = \frac{k_0^2 T^4}{2} e^{\pm 2\beta}\left(1 + \left(\frac{2}{\omega T}\right)^2\right), \tag{27}$$

respectively. Here

$$\theta_c = 2\arctan\left(\frac{\omega T}{2}\right), \tag{28}$$

In general, $\mathrm{Var}(\hat{G}(T))$ and therefore $F_Q^{\mathcal{I}}$ in Eq. 7 exhibits *symmetry* about $\mathrm{Re}(\alpha) = 0$ only when $\theta_c = \pi/2$ for $\omega T = 2$. In the "Doppler" scenario, the expression of $F_Q^{\mathcal{D}}$ (Eq. 8) does not admit further analytical simplification and therefore requires numerical evaluation, even for a Gaussian input state (Eq. 22).

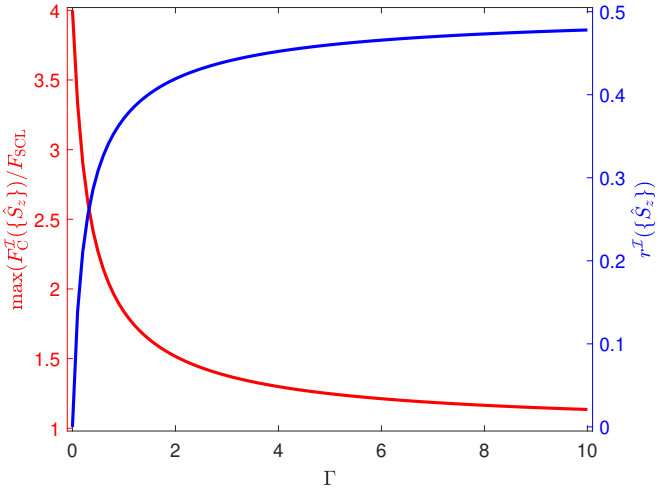


FIG. 2. (color online) In the "Ideal" scenario, the global maximum CFI for population measurement ($F_C^{\mathcal{I}}\{\hat{S}_z\}$, left axis) and the corresponding optimal interrogation-time ratio $r^{\mathcal{I}}(\{\hat{S}_z\})$ (right axis) versus Γ in Eq. 29.

Because both the encoding scheme (input state) and the decoding scheme (measurement protocol) are fixed in our KC atom interferometer, maximizing the sensitivity gain is equivalent, through Eq. 13, to maximizing the corresponding CFI over the control parameters, including the interrogation-time ratio $r = T_1/T$ and the laser phases ϕ_j [64–68]. Specifically, using the single-particle QFI/CFI framework developed in Sec. II, we maximize the corresponding CFI over the relevant control parameters whenever direct optimization is computationally feasible. For joint population–position measurement in the "Doppler" scenario, we instead evaluate the CFI using the control parameters optimized in the "Ideal" scenario, as explained in Sec. III B. The corresponding QFIs are then evaluated at the same control parameters, including the interrogation-time ratio and laser-phase differences. Using this framework, we compare the two measurement protocols in both scenarios, optimize their control parameters whenever direct optimization is computationally feasible, quantify the resulting sensitivity gains and Doppler-induced degradation, and assess the effects of finite spatial detection resolution.

A. Population measurement

In a KC atom interferometer with population measurement, as seen in Eq. 14, the maximum sensitivity is governed by a competition between the gravitational phase response associated with the space–time area difference $\Delta S = \frac{\hbar k_0}{m}|\frac{T^2}{2} - T_2^2|$ [69] and the interference contrast which is exponentially affected by the timing-asymmetry $T_1 \neq T_2$ or equivalently interrogation-time ratio $r \neq 1/2$. The gravitational phase response favors an optimal ratio around $r = 0$ or $r = 1$, whereas the interference contrast

favors $r \approx 1/2$. Therefore, the conventional ratio $r = 1/2$ is not always optimal for MSS inputs.

In the "Ideal" scenario, the CFI for population measurement is determined by the contrast $\mathcal{C} = \exp(-(1-2r)^2\Gamma)$ for MSS (Eq. 15) with

$$\Gamma = \frac{\sigma_p^2}{\sigma_T^2}\left(\left(e^{\beta}\sin(\theta/2)\right)^2 + \left(e^{-\beta}\cos(\theta/2)\right)^2\right). \quad (29)$$

In general, one can show that $F_C^{\mathcal{I}}(\{\hat{S}_z\})$ (Eq. 14) reaches an extremum when

$$r = 2\Gamma(1-2r)(1-2r^2), \quad (30)$$

is satisfied. The solution that maximizes $F_C^{\mathcal{I}}(\{\hat{S}_z\})$ is denoted by $r^{\mathcal{I}}(\{\hat{S}_z\})$. Two features are worth noting: (i) both Γ and $F_C^{\mathcal{I}}(\{\hat{S}_z\})$ (Eq. 14) are *symmetric* about $\mathrm{Im}(\alpha) = 0$; (ii) the *symmetry* about $r = 1/2$ is also broken by phase coherence.

By numerically solving Eq. 30 and maximizing the CFI, the evolutions of $\max(F_C^{\mathcal{I}}(\{\hat{S}_z\}))$ and $r^{\mathcal{I}}(\{\hat{S}_z\})$ versus Γ are shown simultaneously in Fig. 2. In the absence of squeezing ($\beta = 0$ for any θ), $\Gamma = \sigma_p^2/\sigma_T^2$ which usually satisfies $\Gamma \gg 1$, so that an optimal ratio $r \approx 1/2$ is chosen with $F_C^{\mathcal{I}}(\{\hat{S}_z\}) \approx F_{\mathrm{SCL}}$ in a conventional setup. This behavior prevails over most of the parameter space (β, θ) (see the (blue, yellow) regime in Fig. 3 (a1,b1)) because the interference contrast usually dominates the competition. However, around the $\theta = 0$ sector, the dominant factor is the phase coherence of two interference arms because position uncertainty (atomic coherence length) can be exponentially enhanced while the momentum broadening remains small as β increases [70]. Although the parameter regime in which $\max(F_C^{\mathcal{I}}(\{\hat{S}_z\}))$ becomes larger than F_{SCL} is very narrow, we find that by reducing Γ to zero (or equivalently increasing the atomic coherence length), the $\max(F_C^{\mathcal{I}}(\{\hat{S}_z\}))$ (the red solid line in Fig. 2 and the yellow regime in Fig. 3(a1)) can reach the global maximum $4F_{\mathrm{SCL}}$ while $r^{\mathcal{I}}(\{\hat{S}_z\}) \to 0$, as depicted in Fig. 2.

In the "Doppler" scenario where Doppler effects are fully taken into account, however, the maximum CFI $\max(F_C^{\mathcal{D}}(\hat{S}_z))$, and hence the corresponding sensitivity gain, is generally further reduced. As θ moves away from $\theta = 0$ and approaches $\theta = \pi$ for a fixed β, the CFI eventually falls significantly below F_{SCL}. This degradation arises because strong momentum fluctuations severely reduce the phase coherence of the two interference arms. For the optimal interrogation-time ratio, we have numerically checked that the difference between the optimal ratios $r^{\mathcal{I}}(\{\hat{S}_z\})$ and $r^{\mathcal{D}}(\{\hat{S}_z\})$ is small (Fig. 3 (a2,b2)). For QFI, we numerically find that the absolute magnitude of the QFI difference $\Delta F_{\mathrm{Q}} = F_{\mathrm{Q}}^{\mathcal{D}} - F_{\mathrm{Q}}^{\mathcal{I}}$ remains bounded (Fig. 3 (b3)) even under strong Doppler broadening, e.g. $k_0\Delta p/(m\Omega) \approx 0.4$ when $\beta = 4.0$, $\theta = \pi$ and $\sigma_p/(\hbar k_0) = 0.1$. However, around the regimes $\theta = \theta_c = \pi/2$ (the deep blue regime in Fig. 3(a3)) where $F_{\mathrm{Q}}^{\mathcal{I}} \approx F_{\mathrm{SCL}}$, the relative magnitude of the QFI difference is large enough to be relevant, see Fig. 3 (a3,b3).

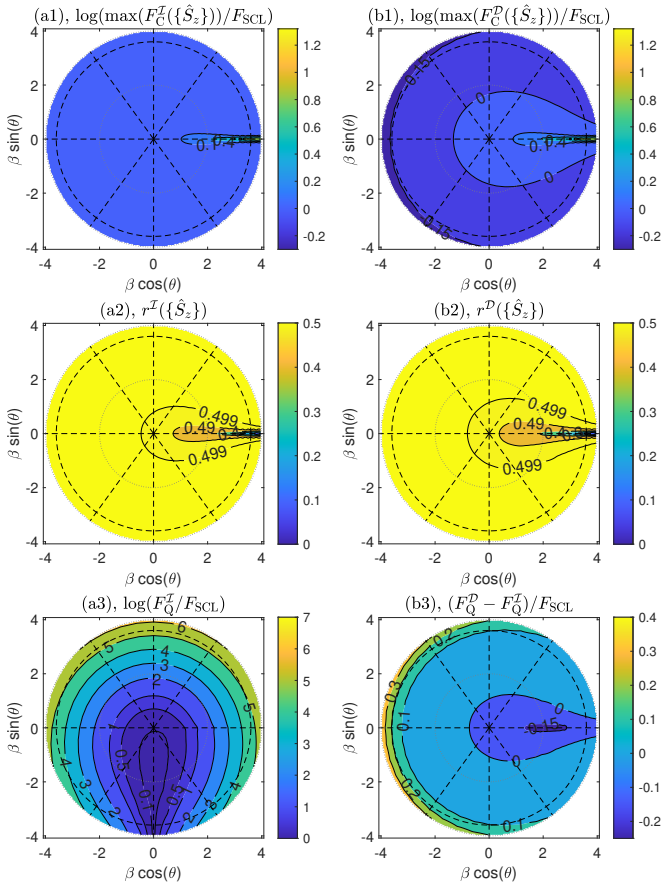


FIG. 3. (color online) Evolution of the maximum $F_C^{\mathcal{S}}(\{\hat{S}_z\})$ under population measurement ((a1,b1), log scale), the optimal interrogation-time ratio $r^{\mathcal{S}}(\{\hat{S}_z\})$ (a2,b2) and the corresponding QFI $F_{\mathrm{Q}}^{\mathcal{S}}$ (a3,b3) versus squeezing parameters (β, θ) for the "Ideal" ($\mathcal{S} = \mathcal{I}$) and "Doppler" ($\mathcal{S} = \mathcal{D}$) scenarios. The black dashed radial lines (concentric circles) correspond to $\theta/\pi = (0, 0.3, 0.5, 0.7, 1.0, 1.3, 1.7, 2)$ ($\beta = 3.6$). Here $\delta_0 = -E_{\mathrm{r}}$, $\Omega = 20E_{\mathrm{r}}/\hbar$, $\omega T = 2$, $T = 200\hbar/E_{\mathrm{r}}$.

B. Joint population–position measurement

In this subsection, we show that the sensitivity of a KC atom interferometer under joint population–position measurement is greatly enhanced by the quantum fluctuations of the input MSS. More importantly, this enhancement remains robust over a sizable parameter region against strong Doppler effects even when imperfect atom–light interactions are fully accounted for. According to Eq. 13, the CFI enhancement discussed below directly determines the corresponding sensitivity gain.

In the "Ideal" scenario, as in the previous subsection, the atom–light interaction is perfect, the spatial distribution of $|s\rangle$ in the falling frame z_0 can be expressed as follows,

$$P_{a/b}(z) \propto e^{-\frac{z_s^2+4z^2}{4\tilde{\Delta}_z^2}}\left(\cosh\left(\frac{z_s z}{\tilde{\Delta}_z^2}\right) \pm \cos(\tilde{k}z + \varphi)\right), \quad (31)$$

here $z_s = \hbar k_0(T_1 - T_2)/m$ denotes the spatial separation between the two output squeezed Gaussian wave packets, whose width is

$$\tilde{\Delta}_z = \sqrt{\frac{\hbar}{m\tilde{\omega}}\Big((\tilde{\omega}\tilde{T})^2 + 1\Big)}, \tag{32}$$

and whose effective wave-number $\tilde{k}$ of the interference pattern is

$$\tilde{k} = k_0 \frac{T_1 - T_2}{\tilde{T}} \frac{(\tilde{\omega}\tilde{T})^2}{1 + (\tilde{\omega}\tilde{T})^2}. \tag{33}$$

In fact, the effect of the MSS can be attributed to the effective modifications of the width $\tilde{\Delta}_z$ and the wavenumber $\tilde{k}$ as follows,

$$\tilde{T} = T + \frac{1}{\omega}\frac{2R\sin(\theta)}{1 + R^2 - 2R\cos(\theta)}, \tag{34}$$

$$\frac{1}{\tilde{\omega}} = \frac{1}{\omega}\frac{1 - R^2}{1 + R^2 - 2R\cos\theta}, \tag{35}$$

$R = \tanh(\beta)$. For comparison, the case of $\beta = 0$ corresponds to $\tilde{\Delta}_z = \sqrt{\hbar\big((\omega T)^2 + 1\big)/(m\omega)}$ and $\tilde{k} = k_0 \frac{T_1 - T_2}{T} \frac{(\omega T)^2}{1+(\omega T)^2}$. Notably, Eq. 34 is *asymmetric* about the real axis of Poincaré disk, $\mathrm{Im}(\alpha) = 0$. To be concrete, both the width $\tilde{\Delta}_z$ and the interference-pattern wavelength $2\pi/\tilde{k}$ in the lower half-plane of the Poincaré disk ($\theta \in (\pi, 2\pi)$) are smaller than those in the upper half-plane ($\theta \in (0, \pi)$), therefore, the sensitivity in the former region is generally larger than that in the latter, see Fig. 4(a1). As a consequence of this asymmetry, the corresponding optimal ratio $r^{\mathcal{I}}(\{\hat{z}, \hat{S}_z\})$ (obtained by maximizing Eq. 20 in the "Ideal" scenario) is also *asymmetric* about $\mathrm{Im}(\alpha) = 0$ (Fig. 4(a2)). Particularly, $r^{\mathcal{I}}(\{\hat{z}, \hat{S}_z\})$ in this case can exceed 1/2, unlike the case of population measurement. In summary, both the maximum CFI and the corresponding optimal interrogation-time ratio are asymmetric with respect to $\mathrm{Im}(\alpha) = 0$; through Eq. 13, the associated sensitivity gain inherits the same asymmetry; these behaviors persist in the "Doppler" scenario.

Furthermore, compared with population measurement, the sensitivity of joint population–position measurement is greatly enhanced over a sizable regime under the "Ideal" scenario, as depicted in Fig. 4(a1,a2,a3). However, this large enhancement strongly depends on the angle θ and the amplitude β. Usually, the larger ωT is, the smaller the area of parameter space in which $\max F_{\mathrm{C}}^{\mathcal{I}}(\{\hat{z}, \hat{S}_z\}) \gg F_{\mathrm{SCL}}$, and the angle $\theta_{\max}$ that maximizes the CFI at fixed β lies approximately along $\theta_c + \pi$, i.e., $\omega T = (0.32, 2.0, 12.5)$ corresponds to $\theta_{\max} \approxeq (1.25, 1.7, 1.95)\pi$. As we can see, the region in (β, θ) space in which large sensitivity enhancement is observed usually includes not only large position uncertainty but also momentum uncertainty (Fig. 4(a1)), the latter makes the "Ideal" scenario inaccurate and calls for the "Doppler" treatment. By analogy with thermal Doppler broadening at finite temperature, a critical question arises: to what extent does this large quantum enhancement survive in the presence of strong Doppler-induced suppression?

However, the combination of Doppler effects and the quadratic momentum phase of either output in Eq. 23 makes an accurate and efficient evaluation of Eq. 20 substantially more challenging [54, 55, 71] (see Appendix B for details). As a comparison, Eq. 16 can be evaluated readily even on a laptop because the quadratic momentum phase is eliminated by spatial integration. We denote the optimal control parameters for joint population–position measurement in the "Doppler" scenario by $r^{\mathcal{D}}(\{\hat{z}, \hat{S}_z\})$, $\psi_{12}^{\mathcal{D}}(\{\hat{z}, \hat{S}_z\})$ and $\psi_{23}^{\mathcal{D}}(\{\hat{z}, \hat{S}_z\})$. In this work, to isolate and quantify the Doppler-induced suppression with an MSS under joint population–position measurement, we do not attempt to directly optimize the corresponding control parameters in the "Doppler" scenario. Instead, we adopt the optimal control parameters obtained in the "Ideal" scenario by globally optimizing $F_{\mathrm{C}}^{\mathcal{I}}(\{\hat{z}, \hat{S}_z\})$ (based on Eq. 31), namely, we assume *a priori* $r^{\mathcal{D}}(\{\hat{z}, \hat{S}_z\}) = r^{\mathcal{I}}(\{\hat{z}, \hat{S}_z\})$, $\psi_{12}^{\mathcal{D}}(\{\hat{z}, \hat{S}_z\}) = \Phi^{\mathcal{I}}(\{\hat{z}, \hat{S}_z\})$, and $\psi_{23}^{\mathcal{D}}(\{\hat{z}, \hat{S}_z\}) = 0$. We finally obtain the corresponding CFI (Eq. 20) numerically, using a *hybrid numerical integration scheme* that combines the Gauss–Legendre and Levin-type quadrature (Appendix B).

Panels in Fig. 4(b1,b3) show the corresponding $F_{\mathrm{C}}^{\mathcal{D}}(\{\hat{z}, \hat{S}_z\})$ and $F_{\mathrm{Q}}^{\mathcal{D}}$ in the "Doppler" scenario. As we can see, the competition between quantum enhancement of MSS and Doppler-induced suppression roughly divides the parameter space (β, θ) into three distinct regimes. Here we take $\omega T = 2.0$ (equivalently $\sigma_p/\hbar k_0 = 0.1$) as an example. When $0.7\pi \lesssim \theta \lesssim 1.2\pi$, the Doppler-induced suppression completely dominates, resulting in a similar behavior between the two measurement protocols (both $\max(F_{\mathrm{C}}^{\mathcal{D}}(\{\hat{S}_z\}))$ and $\max(F_{\mathrm{C}}^{\mathcal{D}}(\{\hat{z}, \hat{S}_z\}))$ are reduced far below F_{SCL}). By contrast, the MSS-induced quantum enhancement greatly enlarges the regime in which $\max(F_{\mathrm{C}}^{\mathcal{D}}(\{\hat{z}, \hat{S}_z\})) \gg F_{\mathrm{SCL}}$, approximately $-0.6\pi \lesssim \theta \lesssim 0.2\pi$. This behavior is sharply distinct from that found for population measurement (Fig. 3(b1)). Furthermore, between these regimes, the competition also induces an optimal squeezing parameter $\beta_{\mathrm{opt}}^{\mathcal{D}}$ where $\max(F_{\mathrm{C}}^{\mathcal{D}}(\{\hat{z}, \hat{S}_z\}))$ reaches the maximum by varying β and fixing θ, see the red solid lines in Fig. 4 (b1,b2,b3). Here we show the optimal squeezing $\beta_{\mathrm{opt}}^{\mathcal{D}}$ as a function of θ only in the upper half-plane. A quantitative comparison of the two measurement protocols in both scenarios is provided in Supplemental Notes.

To illustrate the quantum enhancement of MSS and robustness against Doppler-induced suppression under this measurement protocol, we present in Fig. 5 the maximum $F_{\mathrm{C}}^{\mathcal{I},\mathcal{D}}(\{\hat{z}, \hat{S}_z\})$, the corresponding optimal interrogation-time ratio $r^{\mathcal{I}}(\{\hat{z}, \hat{S}_z\})$, and the associated root fidelity $\mathcal{F}$ (Eq. 11) for this measurement under both the "Ideal" and "Doppler" scenarios. Specifically, we either fix $\beta = 3.6$ and scan the angle $\theta \in [0, 2\pi]$ (Fig. 5(a1,a2,a3)), or fix $\theta = \theta_{\max}$ (where $\theta_{\max}$ is defined as the angle at

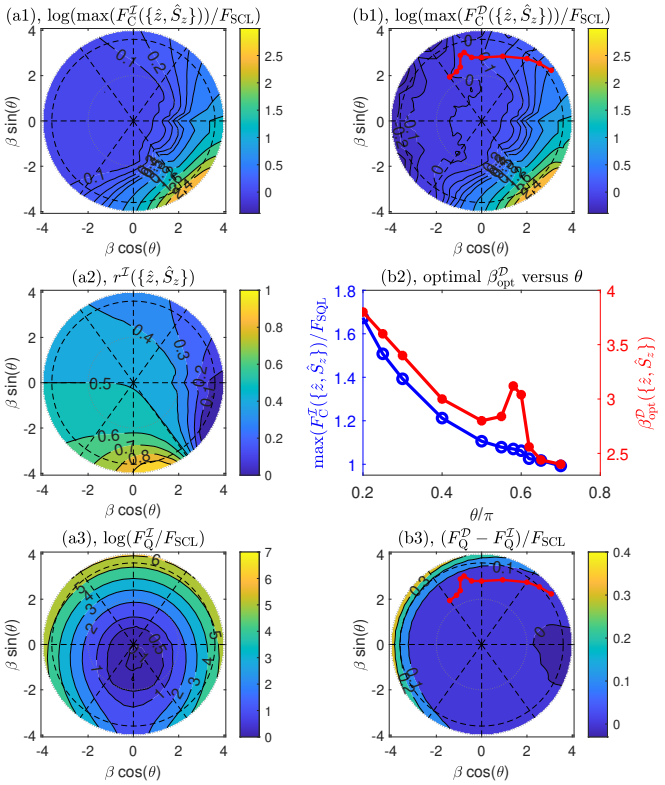


FIG. 4. (color online) Evolution of the maximum $F_C^{\mathcal{S}}(\{\hat{z},\hat{S}_z\})$ of joint population–position measurement ((a1,b1), log scale), the optimal interrogation-time ratio $r^{\mathcal{I}}(\{\hat{z},\hat{S}_z\})$ (a2), and the corresponding QFI $F_Q^{\mathcal{S}}$ (a3,b3) versus squeezing parameters (β,θ) for the "Ideal" ($\mathcal{S}=\mathcal{I}$) and "Doppler" ($\mathcal{S}=\mathcal{D}$) scenarios. In particular, $r^{\mathcal{D}}(\{\hat{z},\hat{S}_z\}) = r^{\mathcal{I}}(\{\hat{z},\hat{S}_z\})$ is assumed for simplicity, as discussed in the main text. Panel (b2) shows the optimal squeezing $\beta_{opt}^{\mathcal{D}}$ (the red solid line in panels (b1,b2,b3)) versus θ ($0 \le \theta \le \pi$ is chosen) in the "Doppler" scenario. The black dashed radial lines (concentric circles) correspond to $\theta/\pi = (0, 0.3, 0.5, 0.7, 1.0, 1.3, 1.7, 2)$ ($\beta = 3.6$). Other parameters are the same as in Fig. 3.

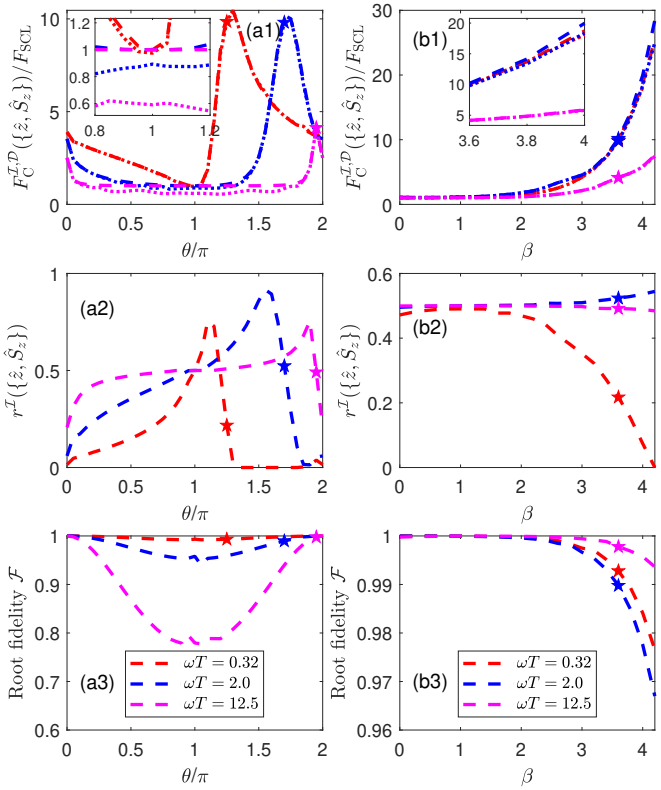


FIG. 5. (color online) Under the joint population–position measurement, the maximum $F_C^{\mathcal{I},\mathcal{D}}(\{\hat{z},\hat{S}_z\})$ (a1, b1), the optimal interrogation-time ratio $r^{\mathcal{I}}(\{\hat{z},\hat{S}_z\})$ (a2, b2), and the root fidelity $\mathcal{F}$ (a3, b3) are shown as functions of the squeezing parameters θ (with $\beta = 3.6$ fixed, panels (a1, a2, a3), see the black dashed circles in Fig. 4) and β (with $\theta = \theta_{max}$ fixed, panels (b1, b2, b3)). Here, the red, blue, and magenta dashed curves (pentagram symbols) correspond to $\omega T = 0.32$, 2.0, and 12.5, respectively. In panels (a1,b1), the dashed (dotted) lines denote the "Ideal" ("Doppler") scenario. Other parameters are the same as in Fig. 3.

which $F_C^{\mathcal{I}}(\{\hat{z},\hat{S}_z\})$ reaches the maximum for a fixed β) and scan $\beta \in [0, 4.2]$ (Fig. 5(b1,b2,b3)). Compared with F_{SCL}, the maximal CFI $\max(F_C^{\mathcal{I},\mathcal{D}}(\{\hat{z},\hat{S}_z\}))$ can be enhanced by roughly one order of magnitude around $\theta = \theta_{max}$ for large enough β (see the pentagrams in Fig. 5), and the Doppler-induced suppression is weak (Fig. 5 (a1,b1)). Although the CFI is only weakly reduced in this regime, Doppler effects noticeably decrease the root fidelity (Eq. 11 and Fig. 5 (a3,b3)). This reduction may be important for practical implementations of MSS-enhanced KC atom interferometers.

C. Finite spatial resolution and experimental assessment

Experimentally, the spatial resolution of detection Δ_{SR} is finite, that is $0 < \Delta_{SR} < \infty$, because of the diffraction limit of detection light and classical noise. In this sense, population measurement (joint population–position measurement) can be understood as the "bad resolution" ("good resolution") detection limit. Therefore, it is useful to model the finite spatial resolution. Here we choose $\beta = 3.6$, $\theta = 1.7\pi$ and $\omega T = 2.0$ as a concrete example (see the blue pentagrams in Fig. 5) to demonstrate the evolution of CFIs as the finite spatial resolution Δ_{SR} is varied, as depicted in Fig. 6. It is worth noting here that a similar assumption on the optimal control parameters is applied for the "Doppler" scenario as in the last subsection. As we can see, the difference between $\max(F_C^{\mathcal{D}}(\{\hat{z},\hat{S}_z\},\Delta_{SR}))$ and $\max(F_C^{\mathcal{I}}(\{\hat{z},\hat{S}_z\},\Delta_{SR}))$ is finite when $\Delta_{SR} \approx 0$, and they quickly converge and simultaneously decay to around F_{SCL} as Δ_{SR} is increased. These behaviors are consistent with the previous results observed in the last two subsections. Actually, both CFIs in the "Ideal" and "Doppler" scenarios are rapidly enhanced when the detection light can resolve the interfer-

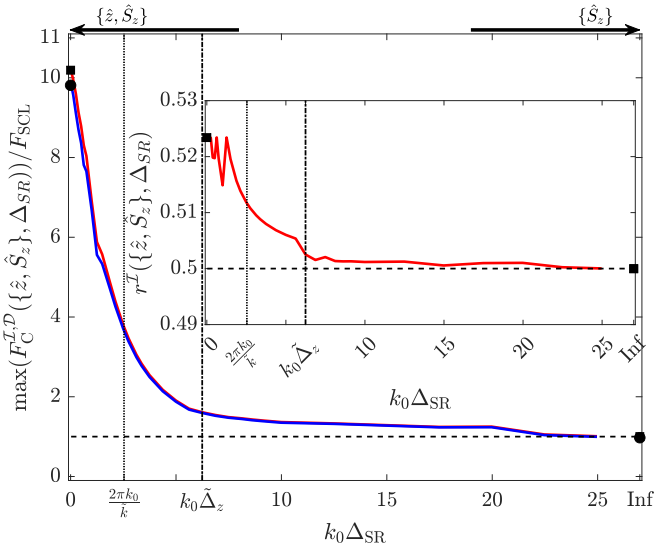


FIG. 6. (color online) The maximum CFIs in the "Ideal" ($\max(F_C^{\mathcal{I}}(\{\hat{z},\hat{S}_z\},\Delta_{SR})$), red solid line) and "Doppler" ($\max(F_C^{\mathcal{D}}(\{\hat{z},\hat{S}_z\},\Delta_{SR})$), blue solid line) scenarios versus finite spatial resolution Δ_{SR}. The black filled squares (circles) correspond to the maximum CFIs in the "Ideal" ("Doppler") scenario for both measurement protocols. The black dashed line corresponds to F_{SCL}, while the black dotted (dashed-dotted) line denotes the case where spatial resolution Δ_{SR} is equivalent to $2\pi/\tilde{k}$ ($\tilde{\Delta}_z$). Here $\beta = 3.6$, $\theta = 1.7\pi$ and $\omega T = 2$, other parameters are the same as in Fig. 5. The inset shows the corresponding interrogation-time ratio $r^{\mathcal{I}}(\{\hat{z},\hat{S}_z\})$ of the "Ideal" scenario versus Δ_{SR}.

ence pattern of the output Gaussian wave packets, that is $\Delta_{SR} \lesssim \tilde{\Delta}_z$ or $\Delta_{SR} \lesssim 2\pi/\tilde{k}$ (see the black dotted or dashed-dotted line in Fig. 6).

Finally, we provide a representative experimental estimate. To retain a CFI enhancement of approximately fourfold or greater at finite spatial resolution, corresponding to a sensitivity gain of approximately *twofold or greater*, and to resolve the Doppler-induced suppression, one must roughly resolve the interference pattern, that is $\Delta_{SR} \lesssim 2\pi/\tilde{k}$, whose characteristic wavelength is reduced by the input MSS. For an alkali-metal atom interferometer, i.e., ^{87}Rb, $T = 200\hbar/E_r \approx 1.1$ millisecond. The wavelength of the detection beam is around 780 nanometers (nm), so the required spatial resolution $\Delta_{SR} \approx 2\pi/\tilde{k} \approx 0.25 \times 780$ nm, which is challenging with current technology [72]. For an alkali-earth-metal(-like) atom interferometer [73], e.g., ^{88}Sr, $T = 200\hbar/E_r \approx 3.4$ milliseconds. The wavelength of the detection beam is around 460 nm, and $\Delta_{SR} \approx 2\pi/\tilde{k} \approx 0.6 \times 460$ nm, so this requirement may become accessible with a high-numerical-aperture imaging system.

IV. CONCLUSION AND OUTLOOK

In conclusion, we have developed a unified single-particle framework for KC atom interferometers with arbitrary uncorrelated motional input states and momentum broadening. For ideal atom–light interactions, the QFI and the CFIs associated with population and joint population–position measurements admit analytical formulations. For Doppler-modified interactions, we derive a comprehensive computational framework for evaluating the corresponding QFI and both CFIs using momentum-dependent pulse operators. In the most demanding case of joint population–position measurement, a hybrid numerical integration scheme resolves the highly oscillatory Fourier-type momentum integrals generated by the interplay between motional position–momentum correlations and nonlinear Doppler coupling. This ideal-to-realistic framework enables the sensitivity enhancement generated by motional squeezing, the performance of different measurement protocols, the optimization of experimentally relevant control parameters where feasible, and Doppler-induced degradation to be assessed within a common quantitative description.

Applied to single-mode motional squeezed states as input, this framework reveals distinct metrological roles of motional squeezing under the two measurement protocols. For population measurement, increasing the atomic coherence length through motional squeezing enables up to a twofold sensitivity enhancement over the semiclassical limit within a narrow position-fluctuation-dominated regime. For joint population–position measurement, the MSS-induced reshaping of spatial interference fringes provides access to additional quantum information encoded in the external degrees of freedom and leads to substantially larger sensitivity gains over a broader squeezing regime. In particular, we identify three characteristic regimes arising from the competition between quantum enhancement and Doppler-induced suppression. In the quantum-enhancement-dominated regime, the sensitivity gain can exceed threefold, remains robust against Doppler-induced suppression under strong momentum broadening, and persists at finite spatial detection resolution. Besides the regime where Doppler-induced suppression dominates, an optimal squeezing strength emerges in the crossover regime where the quantum enhancement and Doppler-induced suppression become comparable. The resulting sensitivity retains standard-quantum-limit scaling, $\delta g \propto N^{-1/2}$, because no many-body entanglement is introduced.

Several challenges remain within the present single-particle setting. First, the CFI for joint population–position measurement in the "Doppler" scenario is currently evaluated using control parameters optimized in the "Ideal" scenario. Developing a more efficient algorithm for the highly oscillatory integrals with stationary points would enable a fully self-consistent Doppler-aware optimization of the interrogation time and laser phases, and thereby determine the true global maxi-

mum of the CFI in the full control-parameter space. Second, large momentum broadening produces Doppler-dependent beam-splitter and mirror imperfections, transferring part of the atomic population out of the intended interferometric paths and eventually reducing the effective number of atoms contributing to the interference signal. This limitation may be mitigated through shaped or modulated pulses [74], Floquet-engineered atom optics [53], or multipath-interference protocols [59]. Third, a realistic implementation should account for intermediate-state decoherence in Raman transitions, residual thermal broadening, imperfect state preparation, detection noise, transverse atomic motion, and residual atom–atom interactions during the interferometric sequence. In this respect, alkaline-earth(-like) platforms [75] employing directly driven narrow optical transitions may offer advantages over Raman-based alkali-metal implementations by avoiding decoherence associated with an intermediate excited state. The principal single-particle predictions of this work could be tested in free-space single-atom matter-wave interferometers [70].

Although the sensitivity gains demonstrated here remain moderate and retain standard-quantum-limit scaling at the single-particle level, the present framework provides a natural starting point for extensions to correlated many-body systems. In particular, the SU(1,1) structure shared by motional squeezed states and certain collective dynamics, including those of two-dimensional interacting Bose gases, suggests that the same information-theoretic approach may be applicable beyond uncorrelated inputs [76, 77]. More generally, combining collective motional correlations with other quantum resources may enable substantially larger metrological gains [78–80]. A systematic investigation of such many-body extensions and their robustness under realistic atom–light interactions is left for future work.

By quantitatively resolving the competition between motional quantum enhancement and Doppler-induced degradation, the present work establishes a benchmark for the future design, control, and performance optimization of atom interferometers based on motional squeezed states [67, 68]. More broadly, our results identify quantum fluctuations of the external motional degrees of freedom as a robust and largely underexplored resource for quantum-enhanced matter-wave interferometry.

V. DATA AVAILABILITY

Datasets generated during the current study are available from the corresponding author on reasonable request.

VI. CODE AVAILABILITY

The underlying code that generate the datasets in this study are available from the corresponding author on reasonable request.

ACKNOWLEDGMENTS

We thank Zhan Zheng for stimulating discussions on motional squeezed states and SU(2) Lie group theory. We thank Yin Zhou and Kanxing Weng for helpful discussions on Kasevich–Chu atom interferometer. We thank Xitao Yu for helpful discussions on the numerical integration of Eq. 20 and for computational support. We also thank Wenqiang Zheng for helpful suggestions on the organization of our manuscript. Fong En Oon was funded by National Science and Technology Major Project for Deep Earth Probe and Mineral Resources Exploration of China (2024ZD1002700). Qiang Lin was funded by National Natural Science Foundation of China (grant Nos. U24A20319, U2341246).

VII. AUTHOR CONTRIBUTIONS

D.Y. initiated the work, and designed the architecture with feedback from all authors. D.Y. developed the methods and performed all analytical calculations and numerical simulations, Y.W. followed and checked part of the results, C.L. helped to figure out the SU(2) and SU(1,1) Lie group. F.E.Oon helped to interpret some of the results. D.Y. and Q.L. supervised the project. D.Y. wrote the main manuscript text. All authors contributed to complete this work and reviewed the manuscript.

VIII. COMPETING INTERESTS

The authors declare no competing interests.

Appendix A: Quantum Fisher information for arbitrary momentum broadening

For the linear frequency chirp $\delta(t) = \delta_0 - k_0 g t$, the unitary operators $\tilde{U}_j^{\mathcal{I},\mathcal{D}}$ becomes independent of the gravitational acceleration g in the freely falling frame. This feature makes it possible to calculate the QFI even in the presence of strong Doppler broadening. The symbolic calculations are performed using *Mathematica* and the package *DiracQ* [81], which enable us to collect, extract and simplify the coefficients as introduced below. According to the definition of QFI, $\frac{F_Q}{4} = \langle \partial_g \Psi(t) | \partial_g \Psi(t) \rangle - |\langle \Psi(t) | \partial_g \Psi(t) \rangle|^2$, the QFI for an arbitrary single-particle input state $|\Psi_0\rangle$ (in the "Doppler" scenario) can be written as follows,

$$\begin{aligned} \frac{F_Q^{\mathcal{D}}}{4} &= \langle \Psi_0 | \hat{c}_0 + \hat{c}_1 \hat{z} + \hat{c}_2 \hat{z}^2 | \Psi_0 \rangle \\ &\quad - |\langle \Psi_0 | \hat{d}_0 + d_1 \hat{z} | \Psi_0 \rangle|^2, \end{aligned} \tag{A1}$$

where both $c_2 = d_1^2$ and $d_1 = mT/\hbar$ are constants, while $\hat{c}_0$, $\hat{c}_1$ and $\hat{d}_0$ solely depend on the momentum operator. These operators can be further expanded around $g = 0$ as follows,

$$\begin{aligned}\hat{c}_0 &= \sum_{j=0}^{2} \hat{c}_{0,j} g^j, \\ \hat{c}_1 &= \sum_{j=0}^{1} \hat{c}_{1,j} g^j, \\ \hat{d}_0 &= \sum_{j=0}^{1} \hat{d}_{0,j} g^j. \end{aligned} \tag{A2}$$

Using the following identities,

$$\begin{aligned}\hat{c}_{0,2} &= d_{0,1}^2, \\ \hat{c}_{0,1} &= 2\hat{d}_{0,0} d_{0,1}, \\ \hat{c}_{1,1} &= 2 d_1 d_{0,1}, \end{aligned} \tag{A3}$$

the QFI in the "Doppler" scenario can be written as follows,

$$\begin{aligned}\frac{F_Q^{\mathcal{D}}}{4} &= \langle\Psi_0|\hat{c}_{0,0} + \hat{c}_{1,0}\hat{z} + \hat{c}_2\hat{z}^2|\Psi_0\rangle \\ &\quad -|\langle\Psi_0|\hat{d}_{0,0} + d_1\hat{z}|\Psi_0\rangle|^2. \end{aligned} \tag{A4}$$

To facilitate comparison with the "Ideal" scenario, it is useful to rewrite the QFI by introducing $\hat{G}'$ and $\hat{G}''$,

$$\begin{aligned}F_Q^{\mathcal{D}} &= k_0^2\left(\frac{T^2}{2} - T_2^2\right)^2 \\ &\quad +4\langle\Psi_0|\hat{G}''|\Psi_0\rangle + 4\mathrm{Var}(\hat{G}'), \end{aligned} \tag{A5}$$

here

$$\hat{G}' = \hat{d}_{0,0} + d_1\hat{z}, \tag{A6}$$

and

$$\begin{aligned}\hat{G}'' &= \hat{c}_{0,0} + \hat{c}_{1,0}\hat{z} + c_2\hat{z}^2 - \hat{G}'^2 - \frac{k_0^2}{16}\left(T^2 - 2T_2^2\right)^2, \\ &= \hat{c}_{0,0} - \hat{d}_{0,0}^2 - i\hbar d_1 \partial_p \hat{d}_{0,0} - \frac{k_0^2}{16}\left(T^2 - 2T_2^2\right)^2, \\ &= \sum_{j=4}^{2}\sum_{i=0}^{4} \hat{G}''_{i,j-i} T_1^i T_2^{j-i}. \end{aligned} \tag{A7}$$

In the final equality, $\hat{G}''$ depends only on the momentum; its explicit dependence on position operator $\hat{z}$ has been eliminated by using the identities in Eq. A3.

Compared with the diagonal terms of $\hat{G}''$, the off-diagonal terms are usually negligible which has been numerically verified. Therefore, $\hat{G}''$ can be approximated as follow,

$$\hat{G}'' \approx \sum_{i=0}^{4} \hat{G}''_{i,4-i} T_1^i T_2^{4-i}, \tag{A8}$$

with

$$\hat{G}''_{0,4} = -k_0^2\left((\frac{1}{2} - \hat{C}_1^2)(\frac{1}{2} - \hat{C}_2^2) - \frac{\hat{\zeta}}{4}\right)^2, \tag{A9}$$

$$\hat{G}''_{1,3} = \frac{k_0^2}{2}\left(\hat{\zeta}'(\hat{C}_2^2 - \frac{1}{2}) - (\hat{C}_1^2 - \frac{1}{2})\hat{\zeta} + \frac{1}{2}\right), \tag{A10}$$

$$\hat{G}''_{2,2} = \frac{k_0^2}{4}\left(\hat{\zeta}'(\hat{C}_2^2 - \frac{3}{2}) - (\hat{C}_1^2 - \frac{1}{2})\hat{\zeta} - \frac{1}{2}\right), \tag{A11}$$

$$\hat{G}''_{3,1} = -k_0^2(\frac{1}{2} - \hat{C}_1^2)^2, \tag{A12}$$

$$\hat{G}''_{4,0} = -\frac{k_0^2}{4}(\frac{1}{2} - \hat{C}_1^2)^2, \tag{A13}$$

$\hat{\zeta} = 4\hat{C}_1\hat{C}_2\,\mathrm{Re}((\hat{A}_1 + i\hat{B}_1)(\hat{A}_2 + i\hat{B}_2)e^{i\hat{\Theta}})$ (Eq. 10), and $\hat{\zeta}' = 4\hat{C}_1^2(\hat{C}_1^2 - 1)$. In the "Ideal" scenario ($\Omega \to \infty$),

$\hat{A}_1 = \frac{1}{\sqrt{2}}$	$\hat{B}_1 = 0$	$\hat{C}_1 = \frac{1}{\sqrt{2}}$
$\hat{A}_2 = 0$	$\hat{B}_2 = 0$	$\hat{C}_2 = 1,$
$\hat{A}_3 = \frac{1}{\sqrt{2}}$	$\hat{B}_3 = 0$	$\hat{C}_3 = \frac{1}{\sqrt{2}}$

(A14)

so that $\hat{G}''_{i,4-i} = 0$ for $i = 0, \cdots, 4$. Actually, $\hat{G}''_{i,j} = 0$ holds exactly in the "Ideal" scenario. A similar approximation for $\hat{d}_{0,0}$ can also be written as follows,

$$\begin{aligned}\hat{d}_{0,0} &= \sum_{j=2}^{1}\sum_{i=0}^{2} \tilde{d}_{i,j-i} T_1^i T_2^{j-i} \\ &\approx \sum_{i=0}^{2} \tilde{d}_{i,2-i} T_1^i T_2^{2-i}, \end{aligned} \tag{A15}$$

here

$$\begin{aligned}\tilde{d}_{2,0} &= \frac{k_0}{2}(\hat{C}_1^2 + \frac{\hat{p}}{\hbar k_0}), \\ \tilde{d}_{1,1} &= k_0(\hat{C}_1^2 + \frac{\hat{p}}{\hbar k_0}), \\ \tilde{d}_{0,2} &= \frac{\hat{p}}{2\hbar} + \frac{k_0}{2}\left(\hat{C}_1^2 + \hat{C}_2^2 - 2\hat{C}_1^2\hat{C}_2^2 + \frac{\hat{\zeta}}{2}\right). \end{aligned} \tag{A16}$$

As $\Omega \to \infty$, $2\tilde{d}_{2,0}$, $2\tilde{d}_{0,2}$ and $\tilde{d}_{1,1}$ consistently approach to $k_0(\frac{1}{2} + \frac{\hat{p}}{\hbar k_0})$, consequently, $\lim_{\Omega\to\infty} \hat{d}_{0,0} = \frac{k_0 T^2}{4} + \frac{T^2}{2\hbar}\hat{p}$. That is,

$$\lim_{\Omega\to\infty} \hat{G}'' = 0, \tag{A17}$$

$$\lim_{\Omega\to\infty} \hat{G}' = \hat{G} + \frac{k_0 T^2}{4}, \tag{A18}$$

which prove that the QFI in the "Doppler" scenario ($F_Q^{\mathcal{D}}$) approach to the "Ideal" counterpart in the limit $\Omega \to \infty$, as depicted in Fig. 7.

Appendix B: Numerical evaluation of $F_C^{\mathcal{D}}(\{\hat{z}, \hat{S}_z\})$

In this appendix, we provide details of the numerical evaluation of $F_C^{\mathcal{D}}(\{\hat{z}, \hat{S}_z\})$ using a hybrid numerical integration scheme involving Gauss–Legendre and Levin-type quadratures.

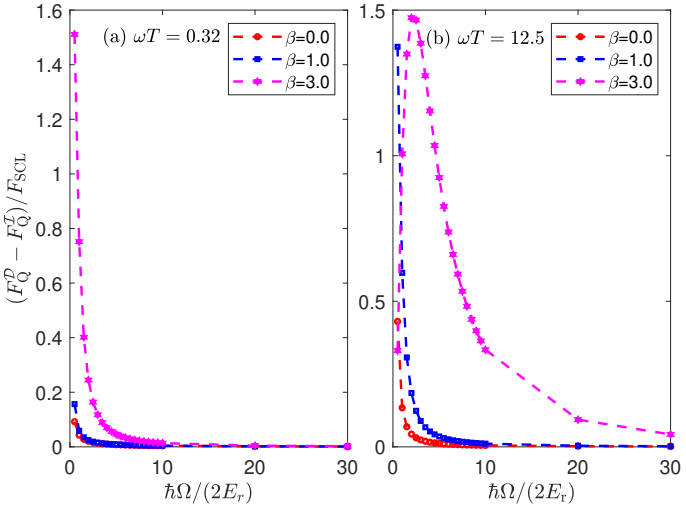


FIG. 7. (color online) Doppler shifts of QFI difference $\Delta F_{\rm Q} = F_{\rm Q}^{\mathcal{D}} - F_{\rm Q}^{\mathcal{I}}$ versus Rabi frequency Ω as $\omega T = 0.32$ (a) and $\omega T = 12.5$ (b). Here we set the interrogation-time ratio $r = T_1/T = 1/2$ artificially. For the input MSS, $\theta = \pi$ is chosen where the Doppler broadening is the largest and $\beta = (0, 1, 3)$ (dashed red, blue and magenta lines). Other parameters are the same as in Fig. 3.

According to the definitions of $\hat{K}_{sa}$, $\hat{K}'_{sa}$, and $\hat{K}''_{sa}$, both $L_s(z)$ and $H_s(z)$ can be transformed into a unified form,

$$D(z) = \int_{-\infty}^{\infty} dp \frac{K(p)}{\sqrt{2\pi\hbar}} e^{-(iA+B)p^2 + ipz/\hbar} \tag{B1}$$

where A and B depend on the squeezing parameters (β, θ) through

$$A = \frac{\tilde{T}}{2m\hbar}, \tag{B2}$$

and

$$B = \frac{1}{2m\hbar\tilde{\omega}} > 0. \tag{B3}$$

The kernel $K(p)$ can finally be expanded as follows,

$$K(p) = \sum_{j=1}^{N_0} \frac{a_{j,0} a_{j,1}(p)}{\sqrt{2\pi\hbar}} \exp\left(i\tilde{b}_j p + i c_j \bar{\Delta}(p)\right), \tag{B4}$$

where $\bar{\Delta}(p) = \sqrt{1+P^2}$, $P = \frac{k_0}{m\Omega} p + \bar{\delta}$, $\bar{\delta} = \frac{\delta_0 + E_r/\hbar}{\Omega}$, and $\tilde{b}_j = (b_j + z/\hbar)$ depends on the position z. All coefficients $a_{j,0}$, b_j and c_j are independent of the momentum and already obtained analytically, whereas $a_{j,1}(p)$ belongs to the seven-function set as below,

$$\frac{(P \pm \bar{\Delta}(p))^l}{\bar{\Delta}^3(p)}, \text{ for } l = 0,\ 1,\ 2,\ 3. \tag{B5}$$

The number N_0 depends on the choice of $\hat{K}_{sa}$, $\hat{K}'_{sa}$ or $\hat{K}''_{sa}$. This integral defining $D(z)$ exhibits three key features: (i) a highly oscillatory factor, $\exp(-iAp^2)$ where the phase is quadratic in p; (ii) a momentum-dependent nonlinear phase, $\exp(ic_j\bar{\Delta}(p))$; (iii) the analytic continuation of $a_{j,1}(p)$ into the complex plane is multivalued and spans multiple Riemann sheets. The second feature (ii) precludes a closed-form evaluation based on standard Gaussian integral identities, while the third (iii) renders analytic continuation into the complex plane prohibitively complicated, preventing any straightforward contour deformation to suppress the oscillatory term. Moreover, due to the first feature (i), standard Fourier transform techniques may become inefficient because prohibitively fine momentum grids are required when $|A| \gg B$.

To numerically obtain the CFI in Eq. 20 or equivalently Eq. B1 especially for an MSS input of large momentum broadening, we employ a hybrid numerical integration scheme combining domain decomposition and Levin-type quadrature [54, 55]. We first divide the momentum integral at the point $P = 0$, which gives $p_0 = -m(\delta_0 + E_r/\hbar)/k_0$. Consequently,

$$D = \sum_{j=1}^{N_0} \int_{-\infty}^{p_0} dp e^{i\phi_L(p)} f_L(p) + \int_{p_0}^{\infty} dp e^{i\phi_R(p)} f_R(p), \tag{B6}$$

and

$$f_L(p) = \frac{a_{j,0} a_{j,1}(p)}{\sqrt{2\pi\hbar}} e^{-Bp^2} e^{ic_j(\bar{\Delta}(p)+P)},$$
$$f_R(p) = \frac{a_{j,0} a_{j,1}(p)}{\sqrt{2\pi\hbar}} e^{-Bp^2} e^{ic_j(\bar{\Delta}(p)-P)}. \tag{B7}$$

In this formula, the kernels $f_{\rm L,R}(p)$ are smooth functions of p that do not contain any highly oscillatory term due to $\lim_{p\to-\infty} \bar{\Delta}(p) + P = 0$ and $\lim_{p\to\infty} \bar{\Delta}(p) - P = 0$. By contrast, the phases $\phi_{\rm L,R}(p)$ are now at most quadratic polynomials of the momentum p,

$$\phi_L(p) = -c_j\bar{\delta} + (b_j + \frac{z}{\hbar} - \frac{k_0}{m\Omega} c_j)p - Ap^2,$$
$$\phi_R(p) = +c_j\bar{\delta} + (b_j + \frac{z}{\hbar} + \frac{k_0}{m\Omega} c_j)p - Ap^2. \tag{B8}$$

Accordingly, two stationary points are defined as follows, $\frac{d\phi_L(p)}{dp}|_{p=p_{L,*}} = 0$ and $\frac{d\phi_R(p)}{dp}|_{p=p_{R,*}} = 0$, with

$$p_{L,*} = \frac{b_j + \frac{z}{\hbar} - \frac{k_0}{m\Omega} c_j}{2A},\ p_{R,*} = \frac{b_j + \frac{z}{\hbar} + \frac{k_0}{m\Omega} c_j}{2A}. \tag{B9}$$

The integral for $D(z)$ (Eq. B1) can then be evaluated within a unified numerical framework. Near a stationary point, the phase varies slowly and is locally dominated by its quadratic expansion, allowing accurate evaluation by Gauss–Legendre quadrature. Away from stationary points, Levin-type quadrature efficiently handles the rapid oscillations [71].

In the following, we briefly introduce the Levin-type quadrature,

$$\mathcal{L} = \int_{p_d}^{p_u} dp e^{i\phi(p)} f(p), \tag{B10}$$

where the stationary point of the phase $\phi(p)$ is assumed to lie outside the interval (p_d, p_u). This integral can be obtained by

$$\mathcal{L} = F(p_u)e^{i\phi(p_u)} - F(p_d)e^{i\phi(p_d)}, \tag{B11}$$

provided that the first-order differential equation for $F(p)$ is solved numerically [54],

$$\frac{dF(p)}{dp} + i\frac{d\phi(p)}{dp}F(p) = f(p). \tag{B12}$$

The differential equation for $F(p)$ can be solved numerically by expanding it in truncated Chebyshev polynomials as follows,

$$F(p) = \sum_{j=0}^{M} \tilde{c}_j T_j(x), \tag{B13}$$

here $p = \frac{p_u+p_d}{2} + \frac{p_u-p_d}{2}x$ and $T_j(x)$ is the jth Chebyshev polynomial of the first kind. Usually, Clenshaw–Curtis nodes are chosen [82], $x_k = -\cos(\pi\frac{k}{N})$, $k = 0, \cdots, N$. Therefore,

$$\sum_{j=0}^{M} \tilde{c}_j \Big(T_j'(x_k) + i\tilde{\phi}'(x_k)T_j(x_k)\Big) = \frac{p_u - p_d}{2}\tilde{f}(x_k), \tag{B14}$$

here $T_j'(x)$ denotes the derivative of $T_j(x)$ with respect to x, $\tilde{\phi}'(x) \equiv \frac{d\phi(p)}{dx}$, $\tilde{f}(x) \equiv f(p)$. We choose $N \approx 3M$ to balance numerical accuracy and computational cost. Because the collocation system is overdetermined for $N > M$, the coefficients $\tilde{c}_j$ are obtained by a least–squares solution. Eq. B12 then yields the integral from the endpoint values $F(p_d)$ and $F(p_u)$. In Fig. 8, we present a benchmark of $F_C^{\mathcal{D}}(\{\hat{z}, \hat{S}_z\})$ versus the truncation order of Chebyshev polynomials M and the truncation order of Gauss–Legendre quadrature n. As we can see, $F_C^{\mathcal{D}}(\{\hat{z}, \hat{S}_z\})$ saturates around $M = 40$, while the result is essentially converged with respect to the Gauss–Legendre order over the range shown. Throughout this work, we evaluate the numerical integral of Eq. 20 with $M = 50$ and $n = 60$.

[1] T. Berrada, S. van Frank, R. Bücker, T. Schumm, J.-F. Schaff, and J. Schmiedmayer, Integrated mach–zehnder interferometer for bose–einstein condensates, Nature Communications **4**, 2077 (2013).

[2] K. S. Hardman, P. J. Everitt, G. D. McDonald, P. Manju, P. B. Wigley, M. A. Sooriyabandara, C. C. N. Kuhn, J. E. Debs, J. D. Close, and N. P. Robins, Simultaneous precision gravimetry and magnetic gradiometry with a bose-einstein condensate: A high precision, quantum sensor, Phys. Rev. Lett. **117**, 138501 (2016).

[3] Z. Fu, B. Wu, B. Cheng, Y. Zhou, K. Weng, D. Zhu, Z. Wang, and Q. Lin, A new type of compact gravimeter for long-term absolute gravity monitoring, Metrologia **56**, 025001 (2019).

[4] N. Heine, J. Matthias, M. Sahelgozin, W. Herr, S. Abend, L. Timmen, J. Müller, and E. M. Rasel, A transportable quantum gravimeter employing delta-kick collimated bose–einstein condensates, The European Physical Journal D **74**, 174 (2020).

[5] M. Kasevich and S. Chu, Measurement of the gravitational acceleration of an atom with a light-pulse atom interferometer, Applied Physics B Photophysics and Laser Chemistry **54**, 321–332 (1992).

[6] D. S. Weiss, B. C. Young, and S. Chu, Precision measurement of $\hbar/m_{\mathrm{Cs}}$ based on photon recoil using laser-cooled atoms and atomic interferometry, Applied Physics B Lasers and Optics **59**, 217–256 (1994).

[7] Y. Bidel, N. Zahzam, C. Blanchard, A. Bonnin, M. Cadoret, A. Bresson, D. Rouxel, and M. F. Lequentrec-Lalancette, Absolute marine gravimetry with matter-wave interferometry, Nature Communications **9**, 627 (2018).

[8] J.-Y. Zhang, W.-J. Xu, S.-D. Sun, Y.-B. Shu, Q. Luo, Y. Cheng, Z.-K. Hu, and M.-K. Zhou, A car-based portable atom gravimeter and its application in field gravity survey, AIP Advances **11**, 115223 (2021).

[9] H. Wang, K. Wang, Y. Xu, Y. Tang, B. Wu, B. Cheng, L. Wu, Y. Zhou, K. Weng, D. Zhu, P. Chen, K. Zhang, and Q. Lin, A truck-borne system based on cold atom gravimeter for measuring the absolute gravity in the field, Sensors **22**, 6172 (2022).

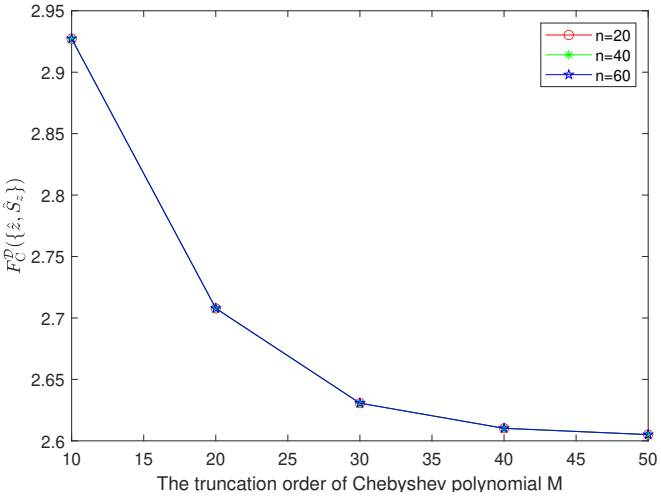


FIG. 8. (color online) Benchmark of $F_C^{\mathcal{D}}(\{\hat{z}, \hat{S}_z\})$ versus the truncation order of Chebyshev polynomial M and the truncation order of Gauss–Legendre quadrature n. Here $\beta = 4.6$ and $\theta = 3\pi/2$. Other parameters are the same as in the main text. As a stringent test, we choose $\beta = 4.6$, beyond the parameter range considered in the main text, to benchmark the hybrid numerical integration scheme in a more demanding a demanding oscillatory regime.

[10] C.-Y. Li, J.-B. Long, M.-Q. Huang, B. Chen, Y.-M. Yang, X. Jiang, C.-F. Xiang, Z.-L. Ma, D.-Q. He, L.-K. Chen, and S. Chen, Continuous gravity measurement with a portable atom gravimeter, Physical Review A **108**, 032811 (2023).

[11] P. Chen, S. Peng, J. Wang, M. Gao, X. Lv, D. Yang, Z. Jin, Y. Wang, X. Tang, B. Wu, X. Wang, B. Cheng, and Q. Lin, An airborne design of inertial stabilized platform for cold atom gravimeter, IEEE Sensors Journal **25**, 13102–13116 (2025).

[12] J. Ma, X. Wang, C. Sun, and F. Nori, Quantum spin squeezing, Physics Reports **509**, 89–165 (2011).

[13] M. H. Schleier-Smith, I. D. Leroux, and V. Vuletić, States of an ensemble of two-level atoms with reduced quantum uncertainty, Phys. Rev. Lett. **104**, 073604 (2010).

[14] C. Brif, B. P. Ruzic, and G. W. Biedermann, Characterization of errors in interferometry with entangled atoms, PRX Quantum **1**, 010306 (2020).

[15] F. Anders, A. Idel, P. Feldmann, D. Bondarenko, S. Loriani, K. Lange, J. Peise, M. Gersemann, B. Meyer-Hoppe, S. Abend, N. Gaaloul, C. Schubert, D. Schlippert, L. Santos, E. Rasel, and C. Klempt, Momentum entanglement for atom interferometry, Phys. Rev. Lett. **127**, 140402 (2021).

[16] L. Salvi, N. Poli, V. Vuletić, and G. M. Tino, Squeezing on momentum states for atom interferometry, Physical Review Letters **120**, 033601 (2018).

[17] G. P. Greve, C. Luo, B. Wu, and J. K. Thompson, Entanglement-enhanced matter-wave interferometry in a high-finesse cavity, Nature **610**, 472–477 (2022).

[18] D. Linnemann, H. Strobel, W. Muessel, J. Schulz, R. J. Lewis-Swan, K. V. Kheruntsyan, and M. K. Oberthaler, Quantum-enhanced sensing based on time reversal of nonlinear dynamics, Phys. Rev. Lett. **117**, 013001 (2016).

[19] I. Kruse, K. Lange, J. Peise, B. Lücke, L. Pezzè, J. Arlt, W. Ertmer, C. Lisdat, L. Santos, A. Smerzi, and C. Klempt, Improvement of an atomic clock using squeezed vacuum, Physical Review Letters **117**, 143004 (2016).

[20] H. Müntinga, H. Ahlers, M. Krutzik, A. Wenzlawski, S. Arnold, D. Becker, K. Bongs, H. Dittus, H. Duncker, N. Gaaloul, C. Gherasim, E. Giese, C. Grzeschik, T. W. Hänsch, O. Hellmig, W. Herr, S. Herrmann, E. Kajari, S. Kleinert, C. Lämmerzahl, W. Lewoczko-Adamczyk, J. Malcolm, N. Meyer, R. Nolte, A. Peters, M. Popp, J. Reichel, A. Roura, J. Rudolph, M. Schiemangk, M. Schneider, S. T. Seidel, K. Sengstock, V. Tamma, T. Valenzuela, A. Vogel, R. Walser, T. Wendrich, P. Windpassinger, W. Zeller, T. van Zoest, W. Ertmer, W. P. Schleich, and E. M. Rasel, Interferometry with bose-einstein condensates in microgravity, Physical Review Letters **110**, 093602 (2013).

[21] S. A. Haine, J. Lau, R. P. Anderson, and M. T. Johnsson, Self-induced spatial dynamics to enhance spin squeezing via one-axis twisting in a two-component bose-einstein condensate, Phys. Rev. A **90**, 023613 (2014).

[22] S. S. Szigeti, S. P. Nolan, J. D. Close, and S. A. Haine, High-precision quantum-enhanced gravimetry with a bose-einstein condensate, Phys. Rev. Lett. **125**, 100402 (2020).

[23] J. M. Brown and T. G. Walker, Perspective: Practical atom-based quantum sensors, Phys. Rev. A **112**, 040102 (2025).

[24] A. Peters, K. Y. Chung, and S. Chu, High-precision gravity measurements using atom interferometry, Metrologia **38**, 25–61 (2001).

[25] D. Braun, G. Adesso, F. Benatti, R. Floreanini, U. Marzolino, M. W. Mitchell, and S. Pirandola, Quantum-enhanced measurements without entanglement, Rev. Mod. Phys. **90**, 035006 (2018).

[26] T. Mazzoni, X. Zhang, R. Del Aguila, L. Salvi, N. Poli, and G. M. Tino, Large-momentum-transfer bragg interferometer with strontium atoms, Phys. Rev. A **92**, 053619 (2015).

[27] P. Cladé, S. Guellati-Khélifa, F. m. c. Nez, and F. m. c. Biraben, Large momentum beam splitter using bloch oscillations, Phys. Rev. Lett. **102**, 240402 (2009).

[28] G. D. McDonald, C. C. N. Kuhn, S. Bennetts, J. E. Debs, K. S. Hardman, M. Johnsson, J. D. Close, and N. P. Robins, $80\hbar k$ momentum separation with bloch oscillations in an optically guided atom interferometer, Phys. Rev. A **88**, 053620 (2013).

[29] G. Colangelo, F. Martin Ciurana, G. Puentes, M. W. Mitchell, and R. J. Sewell, Entanglement-enhanced phase estimation without prior phase information, Phys. Rev. Lett. **118**, 233603 (2017).

[30] L. Pezzé and A. Smerzi, Mach-zehnder interferometry at the heisenberg limit with coherent and squeezed-vacuum light, Phys. Rev. Lett. **100**, 073601 (2008).

[31] J. Kong, F. Hudelist, Z. Y. Ou, and W. Zhang, Cancellation of internal quantum noise of an amplifier by quantum correlation, Physical Review Letters **111**, 033608 (2013).

[32] G. Bihlmayer, P. Noël, D. V. Vyalikh, E. V. Chulkov, and A. Manchon, Rashba-like physics in condensed matter, Nature Reviews Physics **4**, 642 (2022).

[33] M. Kritsotakis, S. S. Szigeti, J. A. Dunningham, and S. A. Haine, Optimal matter-wave gravimetry, Phys. Rev. A **98**, 023629 (2018).

[34] Y. Castin and R. Dum, Bose-einstein condensates in time dependent traps, Physical Review Letters **77**, 5315–5319 (1996).

[35] J. Stenger, S. Inouye, A. P. Chikkatur, D. M. Stamper-Kurn, D. E. Pritchard, and W. Ketterle, Bragg spectroscopy of a bose-einstein condensate, Physical Review Letters **82**, 4569–4573 (1999).

[36] M. Morinaga, I. Bouchoule, J.-C. Karam, and C. Salomon, Manipulation of motional quantum states of neutral atoms, Phys. Rev. Lett. **83**, 4037 (1999).

[37] R. Sutherland, S. Burd, D. Slichter, S. Libby, and D. Leibfried, Motional squeezing for trapped ion transport and separation, Physical Review Letters **127**, 083201 (2021).

[38] M. Xin, W. S. Leong, Z. Chen, Y. Wang, and S.-Y. Lan, Rapid quantum squeezing by jumping the harmonic oscillator frequency, Physical Review Letters **127**, 183602 (2021).

[39] W. S. Leong, M. Xin, Z. Chen, Y. Wang, and S.-Y. Lan, Creation of two-mode squeezed states in atomic mechanical oscillators, Physical Review Letters **131**, 193601 (2023).

[40] J. Metzner, A. Quinn, S. Brudney, I. D. Moore, S. C. Burd, D. J. Wineland, and D. T. C. Allcock, Two-mode squeezing and su(1,1) interferometry with trapped ions, Phys. Rev. A **110**, 022613 (2024).

[41] S. Cavazzoni, B. Teklu, and M. G. A. Paris, Frequency estimation by frequency jumps, npj Quantum Information **11**, 174 (2025).

[42] K. Shukla, L. T. H. Ngo, W. C.-W. Huang, and Y.-W.

Liu, Self-excited truncated motional squeezed state in a quasi-2d bose–einstein condensate, AVS Quantum Science **7**, 045001 (2025).
[43] A. M. Kaufman, B. J. Lester, and C. A. Regal, Cooling a single atom in an optical tweezer to its quantum ground state, Phys. Rev. X **2**, 041014 (2012).
[44] V. Bharti, S. Sugawa, M. Kunimi, V. S. Chauhan, T. P. Mahesh, M. Mizoguchi, T. Matsubara, T. Tomita, S. de Léséleuc, and K. Ohmori, Strong spin-motion coupling in the ultrafast dynamics of rydberg atoms, Phys. Rev. Lett. **133**, 093405 (2024).
[45] A. Shinjo, M. Baba, K. Higashiyama, R. Saito, and T. Mukaiyama, Three-dimensional matter-wave interferometry of a trapped single ion, Physical Review Letters **126**, 153604 (2021).
[46] C. M. Caves, Quantum-mechanical noise in an interferometer, Phys. Rev. D **23**, 1693 (1981).
[47] B. C. Sanders, Review of entangled coherent states, Journal of Physics A: Mathematical and Theoretical **45**, 244002 (2012).
[48] L. P. Pitaevskii and A. Rosch, Breathing modes and hidden symmetry of trapped atoms in two dimensions, Phys. Rev. A **55**, R853(R) (1997).
[49] R. Saint-Jalm, P. C. M. Castilho, E. Le Cerf, B. Bakkali-Hassani, J.-L. Ville, S. Nascimbene, J. Beugnon, and J. Dalibard, Dynamical symmetry and breathers in a two-dimensional bose gas, Phys. Rev. X **9**, 021035 (2019).
[50] D. Linnemann, J. Schulz, W. Muessel, P. Kunkel, M. Prüfer, A. Frölian, H. Strobel, and M. K. Oberthaler, Active su(1, 1) atom interferometry, Quantum Science and Technology **2**, 044009 (2017).
[51] Y. Huang, H.-N. Xiong, W. Zhong, B. Liu, and X. Wang, Su(1, 1) squeezed state, Journal of Physics B: Atomic, Molecular and Optical Physics **52**, 185301 (2019).
[52] J. C. Saywell, I. Kuprov, D. Goodwin, M. Carey, and T. Freegarde, Optimal control of mirror pulses for cold-atom interferometry, Physical Review A **98**, 023625 (2018).
[53] T. Wilkason, M. Nantel, J. Rudolph, Y. Jiang, B. E. Garber, H. Swan, S. P. Carman, M. Abe, and J. M. Hogan, Atom interferometry with floquet atom optics, Phys. Rev. Lett. **129**, 183202 (2022).
[54] D. Levin, Fast integration of rapidly oscillatory functions, Journal of Computational and Applied Mathematics **67**, 95–101 (1996).
[55] D. Levin, Analysis of a collocation method for integrating rapidly oscillatory functions, Journal of Computational and Applied Mathematics **78**, 131–138 (1997).
[56] S. L. Braunstein and C. M. Caves, Statistical distance and the geometry of quantum states, Phys. Rev. Lett. **72**, 3439 (1994).
[57] D. Yu and Z. Zheng, Approximate universality and large measurement gain of rabi model in a linear potential under strong doppler broadening, arXiv:2507.12971 [quant-ph] 10.48550/ARXIV.2507.12971 (2025).
[58] B. Cheng, P. Gillot, S. Merlet, and F. Pereira Dos Santos, Influence of chirping the raman lasers in an atom gravimeter: Phase shifts due to the raman light shift and to the finite speed of light, Phys. Rev. A **92**, 063617 (2015).
[59] Y. Wang, J. Glick, T. Deshpande, K. DeRose, S. Saraf, N. Sachdeva, K. Jiang, Z. Chen, and T. Kovachy, Robust quantum control via multipath interference for thousand-fold phase amplification in a resonant atom interferometer, Phys. Rev. Lett. **133**, 243403 (2024).
[60] A. Sugarbaker, S. M. Dickerson, J. M. Hogan, D. M. S. Johnson, and M. A. Kasevich, Enhanced atom interferometer readout through the application of phase shear, Physical Review Letters **111**, 113002 (2013).
[61] S. M. Dickerson, J. M. Hogan, A. Sugarbaker, D. M. S. Johnson, and M. A. Kasevich, Multiaxis inertial sensing with long-time point source atom interferometry, Physical Review Letters **111**, 083001 (2013).
[62] Y.-J. Chen, A. Hansen, G. W. Hoth, E. Ivanov, B. Pelle, J. Kitching, and E. A. Donley, Single-source multiaxis cold-atom interferometer in a centimeter-scale cell, Physical Review Applied **12**, 014019 (2019).
[63] C. Avinadav, D. Yankelev, M. Shuker, O. Firstenberg, and N. Davidson, Rotation sensing with improved stability using point-source atom interferometry, Physical Review A **102**, 013326 (2020).
[64] C. Oh, C. Lee, C. Rockstuhl, H. Jeong, J. Kim, H. Nha, and S.-Y. Lee, Optimal gaussian measurements for phase estimation in single-mode gaussian metrology, npj Quantum Information **5**, 10 (2019).
[65] S. Ataman, Quantum fisher information maximization in an unbalanced interferometer, Physical Review A **105**, 012604 (2022).
[66] S. Zhou, S. Michalakis, and T. Gefen, Optimal protocols for quantum metrology with noisy measurements, PRX Quantum **4**, 040305 (2023).
[67] F. Belliardo, F. Zoratti, F. Marquardt, and V. Giovannetti, Model-aware reinforcement learning for high-performance bayesian experimental design in quantum metrology, Quantum **8**, 1555 (2024).
[68] A. Ullah, O. E. Müstecaplıoğlu, and M. G. A. Paris, Optimizing quantum sensing networks via genetic algorithms and deep learning, Quantum Science and Technology **11**, 015031 (2025).
[69] P. Storey and C. Cohen-Tannoudji, The feynman path integral approach to atomic interferometry. a tutorial, Journal de Physique II **4**, 1999–2027 (1994).
[70] L. P. Parazzoli, A. M. Hankin, and G. W. Biedermann, Observation of free-space single-atom matter wave interference, Physical Review Letters **109**, 230401 (2012).
[71] K. P. Lovetskiy, L. A. Sevastianov, M. Hnatič, and D. S. Kulyabov, Numerical integration of highly oscillatory functions with and without stationary points, Mathematics **12**, 307 (2024).
[72] J. Wang, J. Tong, W. Xie, Z. Wang, Y. Feng, and X. Wang, Enhanced readout from spatial interference fringes in a point-source cold atom inertial sensor, Sensors **23**, 5071 (2023).
[73] L. Hu, E. Wang, L. Salvi, J. N. Tinsley, G. M. Tino, and N. Poli, Sr atom interferometry with the optical clock transition as a gravimeter and a gravity gradiometer, Classical and Quantum Gravity **37**, 014001 (2019).
[74] Y. Luo, S. Yan, Q. Hu, A. Jia, C. Wei, and J. Yang, Contrast enhancement via shaped raman pulses for thermal cold atom cloud interferometry, EUROPEAN PHYSICAL JOURNAL D **70**, 262 (2016).
[75] X. Zhang, R. P. del Aguila, T. Mazzoni, N. Poli, and G. M. Tino, Trapped-atom interferometer with ultracold sr atoms, Physical Review A **94**, 043608 (2016).
[76] C. Lv, R. Zhang, and Q. Zhou, $su(1,1)$ echoes for breathers in quantum gases, Phys. Rev. Lett. **125**, 253002 (2020).
[77] P. Zhang and Y. Gu, Periodically and quasi-periodically

driven dynamics of bose-einstein condensates, SciPost Phys. **9**, 079 (2020).

[78] G. Vallone, E. Pomarico, P. Mataloni, F. De Martini, and V. Berardi, Realization and characterization of a two-photon four-qubit linear cluster state, Phys. Rev. Lett. **98**, 180502 (2007).

[79] B.-C. Ren, F.-F. Du, and F.-G. Deng, Hyperentanglement concentration for two-photon four-qubit systems with linear optics, Phys. Rev. A **88**, 012302 (2013).

[80] A. L. Shaw, P. Scholl, R. Finkelstein, R. B.-S. Tsai, J. Choi, and M. Endres, Erasure cooling, control, and hyperentanglement of motion in optical tweezers, Science **388**, 845–849 (2025).

[81] J. G. Wright and B. S. Shastry, Diracq: A package for algebraic manipulation of non-commuting quantum variables, Journal of Open Research Software **3**, 13 (2015).

[82] A. Iserles and G. Maierhofer, An accelerated levin–clenshaw–curtis method for the evaluation of highly oscillatory integrals, BIT Numerical Mathematics **65**, 36 (2025).

Supplementary Files

This is a list of supplementary files associated with this preprint. Click to download.

- supp.zip